Roughness Characteristics of Oceanic Seafloor Prior to Subduction in Relation to the Seismogenic Potential of Subduction Zones

Serge Lallemand, Michel Peyret, Elenora van Rijsingen, Diane Arcay, Arnauld Heuret

▶ To cite this version:

Serge Lallemand, Michel Peyret, Elenora van Rijsingen, Diane Arcay, Arnauld Heuret. Roughness Characteristics of Oceanic Seafloor Prior to Subduction in Relation to the Seismogenic Potential of Subduction Zones. Geochemistry, Geophysics, Geosystems, 2018, 19 (7), pp.2121-2146. ⟨10.1029/2018GC007434⟩. ⟨hal-01884576⟩

HAL Id: hal-01884576

https://hal.science/hal-01884576v1

Submitted on 1 Oct 2018

Geochemistry, Geophysics, Geosystems

RESEARCH ARTICLE

10.1029/2018GC007434

Key Points:

- We have developed a new database characterizing seafloor roughness seaward of oceanic subduction trenches
- The oceanic seafloor prior to subduction is used as a proxy of the seismogenic subduction interface
- Trench segments are described in terms of short- or long-wavelength parameters
- High seismic coupling is observed when seafloor roughness is relatively low, and low seismic coupling is associated with relatively high roughness subducting seafloor

Supporting Information:

- Supporting Information S1

Correspondence to:
S. Lallemand,
lallem@gm.univ-montp2.fr

Citation:
Lallemand, S., Peyret, M., van Rijsingen, E., Arcay, D., & Heuret, A. (2018). Roughness characteristics of oceanic seafloor prior to subduction in relation to the seismogenic potential of subduction zones. *Geochemistry, Geophysics, Geosystems*, *19*, 2121–2146. https://doi.org/10.1029/2018GC007434

Received 16 JAN 2018
Accepted 5 JUN 2018
Accepted article online 26 JUN 2018
Published online 17 JUL 2018

Roughness Characteristics of Oceanic Seafloor Prior to Subduction in Relation to the Seismogenic Potential of Subduction Zones

Serge Lallemand[1], **Michel Peyret**[1], **Elenora van Rijsingen**[1,2], **Diane Arcay**[1], **and Arnauld Heuret**[3]

[1]Géosciences Montpellier, CNRS, Montpellier University, Montpellier, France, [2]Laboratory of Experimental Tectonics, Roma Tre University, Roma, Italy, [3]Géosciences Montpellier, Guyane University, Cayenne, France

Abstract We have developed a new approach to characterize the seafloor roughness seaward of the trenches, as a proxy for estimating the roughness of the subduction interface. We consider that abrupt elevation changes over given wavelengths play a larger role in the seismogenic behavior of the subduction interface than the amplitude of bathymetric variations alone. The new database, SubRough, provides roughness parameters at selected spatial wavelengths. Here we mainly discuss the spatial distribution of short- (12–20 km) and long-wavelength (80–100 km) roughness, R_{SW} and R_{LW}, respectively, along 250-km-wide strips of seafloor seaward of the trenches. Compared with global trend, seamounts show distinct roughness signature of much larger amplitudes at both wavelengths, whereas aseismic ridges only differ from the global trend at long wavelengths. Fracture zones cannot be distinguished from the global trend, which suggests that their potential effect on rupture dynamics is not the consequence of their roughness, at least not at these wavelengths. Based on R_{LW} amplitude, segments along subduction zones can be defined from rough to smooth. Subduction zones like the Solomons or the Ryukyus appear dominantly rough, whereas others like the Andes or Cascadia are dominantly smooth. The relative contribution of smooth versus rough areas in terms of respective lateral extents probably plays a role in multipatch rupture and thus in the final earthquake magnitude. We observe a clear correlation between high seismic coupling and relatively low roughness and conversely between low seismic coupling and relatively high seafloor roughness.

Plain Language Summary We have developed a new database characterizing the seafloor roughness seaward of oceanic trenches as a proxy of the roughness of the subduction interface with the aim to evaluate how it influences the occurrence of large interplate earthquakes. Counterintuitively, we observe that the coupling between the converging plates is higher when the plate interface is smooth, and the coupling is low when the interface is rough.

1. Introduction

Many studies have emphasized the role of subducting topography in the initiation, propagation, and termination of ruptures of large to mega-earthquakes. As early as in the late 80s, Ruff (1989), based on a limited database, suggested that smooth seafloor associated with excess trench sediment favored large ruptures. Soon after, Cloos (1992) proposed that subducting seamounts were likely candidates for large earthquake triggers. Based on additional marine observations and physical modeling, alternative processes have been proposed involving multiple seismogenic behaviors depending on the type of subducting topographic features (Abercrombie et al., 2001; Bassett & Watts, 2015a, 2015b; Bilek, 2009; Bilek et al., 2003; Carena, 2011; Cloos, 1992; Das & Watts, 2009; Dominguez et al., 2000; Geersen et al., 2015; Gutscher et al., 1999; Henstock et al., 2016; Kodaira et al., 2000; Konca et al., 2008; Kopp, 2013; Landgrebe & Müller, 2015; Marcaillou et al., 2016; Métois et al., 2012; Mochizuki et al., 2008; Morgan et al., 2008; Müller & Landgrebe, 2012; Robinson et al., 2006; Scholz & Small, 1997; Sparkes et al., 2010; Wang & Bilek, 2011, 2014; Yang et al., 2012), the trench sediment thickness (Heuret et al., 2012; Jarrard, 1986; Ruff, 1989; Scholl et al., 2015), the state of stress within the upper plate (Heuret et al., 2012; Jarrard, 1986; Schellart & Rawlinson, 2013), the possible occurrence of tectonic erosion (Bilek, 2010; Sage et al., 2006; Scholl et al., 2015), the friction, normal stress, and fluid pressure along the subduction interface (Chlieh et al., 2011; Corbi et al., 2011; Lin et al., 2013; Ranero et al., 2008; Ruff, 1992; Saffer & Tobin, 2011; Saillard et al., 2017; Scholz, 1998) or the geometry or kinematics of the subduction zone (Bletery et al., 2016; Gutscher & Westbrook, 2009; Jarrard, 1986; McCaffrey, 2008;

Schellart & Rawlinson, 2013; Uyeda, 1987). Some of these studies argue that along-trench segments exhibiting low topographic roughness at long spatial wavelength should be prone to propagate ruptures over large distances and, consequently, be the location of very large earthquakes. On the other hand, subducting highs may—in some circumstances—act as strong patches where stress builds up and suddenly releases or—in other circumstances—act as a barrier to rupture propagation.

Global seafloor roughness characterization intending to compare the data with subduction zone seismicity has already been performed using two different techniques or approaches. Morgan et al. (2008) have used semivariograms built in the spatial domain along 10 subduction segments (on both sides of the trench), which they later compare with 30 $M_w \geqq 7.7$ earthquake events. They concluded that the geomorphology of the subducting seafloor and forearc constrain the earthquake size. Bassett and Watts (2015a, 2015b) have computed and analyzed the residual bathymetric and gravimetric anomalies after removal of the long-wavelength topography and gravity field from subduction zones. In the same manner as Morgan et al., they examined both sides of the trench but at larger distances (600 km on each side instead of ~100 km for Morgan et al.). They observe that subducted features have contrasting expressions in the arc and forearc. Subducting seamounts for example have similar morphological expressions as unsubducted ones, but only at slab depths less than 17 km. Subducting aseismic ridges can be traced in the forearc with a gradual reduction in morphologic expression. In some cases, the authors are able to correlate their signal with the downdip limit of coseismic slip and strong interplate coupling. Preexisting crustal structures over the margin like faults or lateral variations in rigidity significantly influence the seismogenic behavior (Bassett et al., 2016) and superimpose on the subducting seafloor contribution.

However, a homogeneous and worldwide estimate of the oceanic plate roughness prior to subduction is still missing. In this study, we have developed a new database, called SubRough, based on a spatial frequency analysis, which aims at providing a simple and synthetic quantification of the seafloor roughness, which is supposed to play a role in the seismogenic behavior of the subduction interface. Our approach is designed to study the seismogenic effect of subducted reliefs, that may have a dual influence on seismicity, as a function of their characteristic spatial scale. Because there are very few places in the world where we have access to a detailed mapping of the subduction interface, we have decided to use the bathymetry seaward of the trench as a proxy of the currently subducting topography along the seismogenic plate interface. Such an approach has been successfully applied to specific ruptures by Das and Watts (2009), which appear to be controlled by the subducting seafloor topography. We will first explain the novelty of the methodology used for roughness characterization. Then, we will present the SubRough data set and interpret the roughness signal with regard to the expected seismogenic character, focusing on specific features like seamounts, ridges, or fracture zones. We will evaluate to which extent the seafloor roughness controls the state of stress in subduction zones. We will finally discuss the limits and potentials of our approach and propose some extensions of this work, which we believe are worth exploring. A detailed correlation of seafloor roughness with the seismogenic behavior along subduction zones is studied in a companion paper by van Rijsingen et al. (2018).

2. Methodology Used for Roughness Calculation

We have applied the following criteria while constructing the SubRough database:

1. quantifying discrete seafloor roughness for all oceanic subduction zones;
2. defining homogeneity, in both spatial coverage and resolution, in the processed elevation data set, even if higher bathymetric resolution is available for some regions;
3. ascribing a limited number of roughness parameters corresponding to different relevant spatial scales for the purpose of studying large earthquake rupture dynamics.

2.1. Data Sources

Even if high-resolution bathymetric data are available for some specific areas, we used the General Bathymetric Charts of the Oceans (GEBCO) database, released in 2014 (Becker et al., 2009; Sandwell et al., 2002; Smith & Sandwell, 1997; Weatherall et al., 2015) to match the constraint of working at a global scale. This database is gridded at 30″-arc (~1 km) interval. It is a combination of high-resolution (kilometer scale) measurements obtained by echo sounding from ship survey and lower resolution (typically $>$10 km) measurements from satellite gravity anomalies. Its vertical accuracy is on the order of a few hundred meters, while its global resolution is estimated to 12.5 km (Smith & Sandwell, 1997). Our estimate of the vertical error between high- and low-resolution data is ~100 m based on statistics performed on residual bathymetry when subtracting swath-mapping data acquired onboard R/V L'Atalante in 1996 and in 2017 from GEBCO database (standard deviation is 117 m for ACT data east of Taiwan and 55 m for GARANTI data west of Guadeloupe). Since the database contains about 10% of high-resolution data over our zones of interest, we have decided not to take them into account and only provide roughness estimates at wavelengths longer than 12 km for homogeneity over all subduction zones.

2.2. Roughness Definition

The roughness of a surface can be defined as the deviation of its elevation around a mean value. Keeping in mind both the global data resolution and the final objective of providing a limited number of roughness parameters characterizing the ability of the subduction interface to produce large earthquakes, we have elaborated the following technique.

2.2.1. Roughness in the Spatial Domain

In this study, we consider that abrupt elevation changes over short and longer distances likely play a larger role in seismicity initiation, propagation and arrest, than the elevation values (bathymetry) themselves. One may hypothesize that, if the energy released is sufficient, a rupture can propagate, whatever the mean elevation is, as long as no topographic gradient threshold is met. We thus focus on the roughness of the topography R_Ω in meters, which is defined as the deviation (root mean square) of its elevation z around its mean value $\bar{z}$ within a given spatial domain Ω (equation (1); see Text S1 in the supporting information for more details).

$$R_\Omega = \left(\int_\Omega (z - \bar{z})^2 \mathrm{d}\Omega \right)^{1/2} \tag{1}$$

A classical way to estimate this disparity is to perform an autocorrelation of z in the spatial domain. For efficiency, we move the autocorrelation function of the elevation into the frequency domain via Fourier transform leading to the power spectral density (PSD).

2.2.2. Roughness in the Frequency Domain

Given that the total energy of one signal is the same in both the spatial and frequency domain, one can define the roughness in the frequency domain R_f using equation (2), where f_x and f_y are the frequencies in the x and y directions (see Text S1 in the supporting information for more details).

$$R_f = \left[\iint_0^{+\infty} PSD\left(f_x, f_y\right)\, df_x\, df_y \right]^{1/2} \tag{2}$$

2.2.3. Roughness in a Radial Bandwidth

Some authors like Dunham et al. (2011) also define a "bandwidth roughness," which only takes into account the contribution of one specific frequency band (or wavelength band) to the complete deviation of the signal around its zero mean value, either considering specific directions or radial frequencies (see Text S1 in the supporting information for more details). In this study, we will mainly use radial frequencies (Figure 1), by implicitly assuming that the bathymetry deviation is isotropic. The radial frequency bandwidth roughness $R_{?f}$ can be written as

$$R_{\Delta f} = \left[\int_{f_{\min}}^{f_{\max}} PSD(f) df \right]^{1/2} \tag{3}$$

2.2.4. Roughness Parameter Assuming Fractal Model

In order to regularize roughness values, we have the choice to fit discrete PSD measurements with different models. One of them takes into account the fractal structure of topography. It has been shown that global topography on Earth can be considered as a fractal object, that is, the distribution of elevation is similar, regardless of the scale (Renard et al., 2013; Turcotte, 1992). It means that the PSD of topography exhibits a power law dependence on radial frequency (e.g., Fox & Hayes, 1985; Huang & Turcotte, 1989, 1990; Turcotte, 1997; Voss, 1988):

$$PSD(f) \propto |f|^{-(\beta+1)} \tag{4}$$

10.1029/2018GC007434

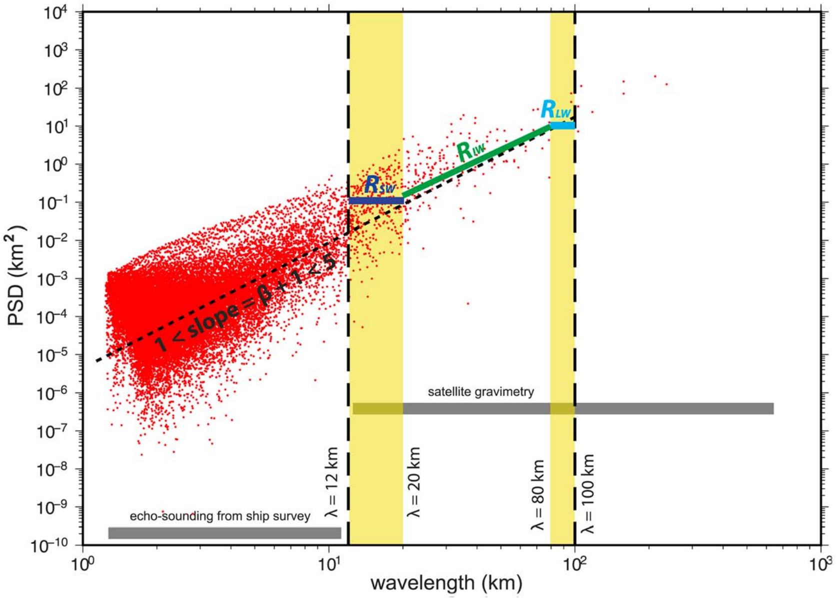

Figure 1. Example of a typical power spectral density graph. Each red point represents one PSD (f) value. The linear regression through this log-log graph represents the fractal model that best fits the PSD function. The fractal model can be estimated over different frequency bands (1–100 km for the dotted black line, 20–80 km for the green line). Mean PSD values over the wavelength bands (12–20 km) and (80–100 km) are shown in dark and light blue, respectively. Because echo sounding from ship survey are rather sparse in the General Bathymetric Charts of the Oceans database, a uniform analysis over all the subduction zones requires considering only wavelengths longer than 12 km (spatial resolution of the satellite gravimetry). PSD = power spectral density.

In a log-log plot, $(\beta + 1)$ is the slope (in absolute value) of the theoretical dependence of PSD values on radial frequency (dotted line in Figure 1). This exponent can also be expressed in terms of other parameters that are commonly used in the literature, such as the fractal dimension (see Text S1 in the supporting information for more details).

Using this fractal model, the roughness parameter defined by equation (3) for a given radial wavelength bandwidth $R_{\Delta\lambda/\mathrm{fractal}}$ and for $\beta > 0$ becomes

$$R_{\Delta\lambda/\mathrm{fractal}} = \left[\frac{C}{\beta}\right]^{1/2} \left(\lambda_{\mathrm{max}}{}^{\beta} - \lambda_{\mathrm{min}}{}^{\beta}\right)^{1/2} \tag{5}$$

where C is a constant and $\lambda = \frac{1}{f}$ is the spatial wavelength. It can be visualized directly in a log-log representation where the PSD between two wavelengths is approximated by a regression line (bold green line in Figure 1).

2.2.5. Roughness Assuming Average Model

Another simpler model to fit the PSD is the average over a given frequency bandwidth. Using the fractal or average model for estimating the roughness generally leads to similar results. Indeed, the PSD exhibits a clear fractal structure almost everywhere. We find a mean slope value (over all the subduction segments) of 2.9, which is similar to what is generally found for topography (e.g., intermediate frequencies in Perron et al., 2008). Nevertheless, we often notice a slightly steeper bending of the PSD graph at high frequencies (typically $\lambda \leq 10$ km). This pattern has already been reported (e.g., Perron et al., 2008). By contrast, a slight reduction in spectral slopes at long wavelength is observed even if no prior detrending step is performed (see bold green line with respect to black dotted line in Figure 1). Moreover, we found a few areas characterized by large variance within particular frequency bands, thus revealing local topography patterns that do not fit with a regional fractal model. In the case of limited frequency bandwidth or limited number of discrete measurements, it appears that the PSD function may be more reliably approximated by the mean value within the considered frequency band (blue lines in Figure 1). Although this approach seems, at least in principle, less integrative than the fractal approach, in practice, it appears to be steadier for narrow wavelength intervals, since the fractal hypothesis may not be valid everywhere.

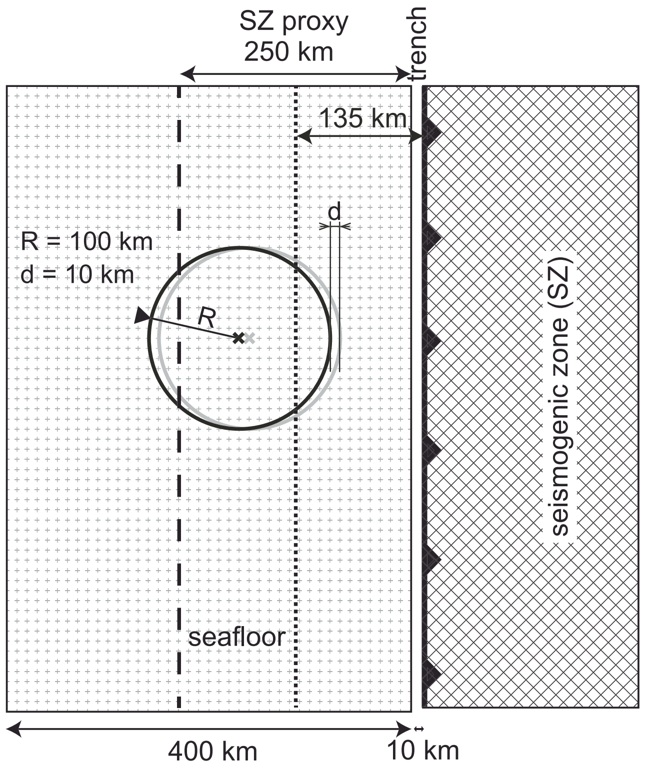

Figure 2. Schematic view of processing. The region of interest is a strip along the trench, 400 km wide, located 10 km seaward the trench. The power spectral density (and roughness) calculation is performed on a circular window (100-km radius). This analysis is done over a uniform spatial grid with 10-km spacing as shown by the dots filling the study area.

Using the average model, the roughness parameter in equation (3) for a given radial wavelength bandwidth $R_{\Delta\lambda/\text{mean}}$ becomes

$$R_{\Delta\lambda/\text{mean}} = \left[\overline{PSD}\right]^{1/2}\left({}^{1}/_{\lambda_{\min}} - {}^{1}/_{\lambda_{\max}}\right)^{1/2} \tag{6}$$

where $\overline{PSD}$ is the mean value of PSD over the wavelength band $[\lambda_{\min}, \lambda_{\max}]$.

2.2.6. Roughness Uncertainties or Disparities

On top of the data resolution discussed above, there are several ways to compute the uncertainty of roughness estimators. The simplest one consists in using the standard deviation of the PSD values σ_{PSD} over some frequency bands when applying the average approach (see Text S1 in the supporting information for details). The second one consists in estimating the standard deviations of the slope and intercept when using the fractal approach but is less easy to derive. We have thus implemented a third approach adapted to both average and fractal models and which relies on the determination of the variance of roughness values over several spatial orientations. This technique is also a way to measure the robustness of the radial/isotropic approach as well as to complement the roughness database with more detailed information related to orientation. We thus systematically performed the roughness calculation along 12 different orientations, with 15° wide opening each, to cover the 0–180° azimuth range. The variance over the 12 orientations constitutes a good proxy for roughness disparity. Roughness estimates for specific orientations are briefly treated in the supporting information (Figure S1). Throughout the rest of this paper, we will only consider radial bandwidth roughness estimators $R_{\Delta\lambda/\text{mean}}$ or $R_{\Delta\lambda/\text{fractal}}$.

2.3. Processing Chain and Choice of Criteria Used for Seafloor Roughness Characterization

2.3.1. Area/Regions Covered

Since the currently subducting topography is generally unknown, we assume that the bathymetry of oceanic plates, a few hundreds of kilometers seaward of the trench, is a reasonable proxy for modeling the roughness of the subduction interface. The roughness analysis has been performed over most oceanic subduction zones. We have not paid much attention to narrow subduction systems or those where continental crust is significantly involved. Based on the location of oceanic trenches from Heuret and Lallemand (2005), we have selected a 400-km-wide strip of seafloor bathymetry 10 km seaward the trench (Figure 2). In many locations, a thick pile of sediment fills the trench and smooths the seafloor before entering the subduction zone. Since we generally do not know how much of the trench fill is scraped off at the margin's front, we avoid being too close to the trench, where trench fill may alter the roughness estimate. Including this 10-km-wide seafloor strip into our calculations would contribute for only 1/40, that is, 2.5% of our results (4% if when focusing on a 250-km-wide strip). In the same way, we do not explore too far away from the trench where direct comparison with the current seismogenic zone behavior becomes very uncertain.

2.3.2. Calculation Steps

2.3.2.1. Extraction of the Relative Bathymetry

The roughness mathematical definition requires that the elevation distribution is a realization of a stationary random field (i.e., spatial stochastic process). We thus first model and remove the plate bending contribution from the bathymetric database. To do so, we average bathymetric profiles spaced by 10 km, perpendicular to the trench (Figure 3), over a sliding 500 km-long trench-parallel window. Beforehand, seamounts are masked using the database of Kim and Wessel (2011), even though their contribution vanishes in the averaging process. Additionally, we also manually mask the main ridges and continental platforms in order to preserve their large-scale topographic signature from the averaging process. When the lateral extent of the subduction segment is smaller than 500 km, the averaging process is performed over the whole segment. This approach is similar to the one used by Bassett and Watts (2015a, 2015b). Once this mean reference bathymetry is

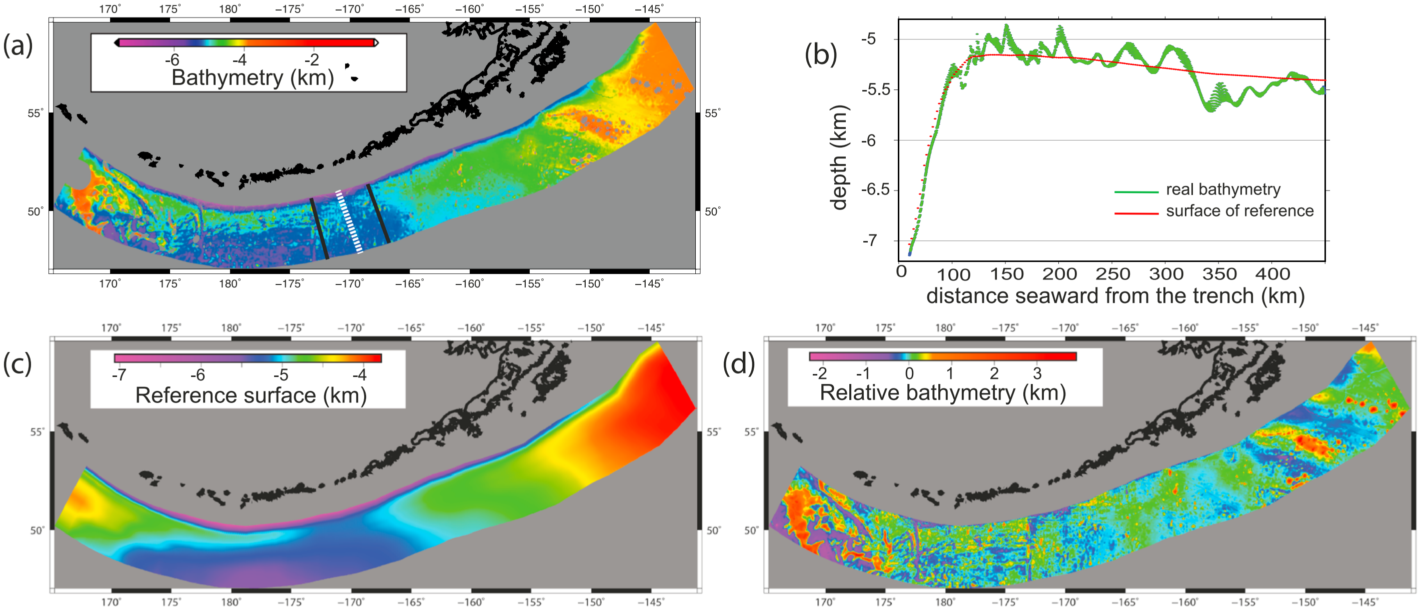

Figure 3. Example of plate bending removal along the Aleutians. (a) Real bathymetry from GEBCO_2014. For estimating the reference surface at white dotted profile, averaging is performed over all profiles perpendicular to the trench that lie between the two black profiles that are 500 km away from each other. Seamounts (in gray) are removed from the bathymetric data set before processing. (b) Elevation (in green) along the white dotted profile shown in (a) and mean elevation over neighboring profiles (in red). (c) Reference surface over the Aleutians. Note the fit to the curvature close to the trench. (d) Relative bathymetry defined as the real bathymetry minus the reference surface.

obtained (Figure 3c), it is subtracted from the real bathymetry, leading to what is called hereafter the relative bathymetry whose statistical mean in the study area is zero (Figure 3d).

2.3.2.2. PSD Calculation

The relative bathymetry data set is projected into a local Cartesian coordinates system, that is, Conic Lambert projection whose origin and standard parallels are adapted to the studied subduction zone. The PSD mapping is performed over all subduction segments discretized by a 10-km square grid (Figure 2). We use a circular sliding window with a radius of 100 km compatible with the width of the strips and allowing for analyzing the seafloor roughness up to a maximum wavelength of 200 km. A local planar detrend is performed in order to remove the null frequency component of the relative bathymetry that, at this small spatial scale, would have not been eliminated in the reference bathymetry. The PSD is calculated on the full-resolution GEBCO data set (30″ ≈ 1 km) even though only wavelengths higher than 12 km are further retained in our roughness analysis as they correspond to the resolution of the bathymetry derived from satellite gravity anomalies (Figure 1).

2.3.2.3. Selection of Frequency Bandwidths

The longest investigated wavelength is given by the diameter of the sliding window, that is, 200 km. In practice, the longer the wavelength is, the fewer the samples are (Figure 1). Thus, considering only wavelengths typically longer than 100 km may lead to unstable results. Keeping in mind these limitations (better sampling between 12 and 100 km wavelengths within a larger data set ranging from 1 to 200 km), the choice of wavelength band limits for roughness calculation is somewhat arbitrary. We aim at discriminating the contribution of various topographic features, whose typical elevation and spatial extent are different, to the global roughness of the subducting plate. When considering short wavelengths, we expect to be sensitive to elevation changes induced by the presence of fracture zones or isolated small seamount. When looking at the longest wavelengths available in our analysis, we are blind to such small topographic patterns but sensitive to larger ones like ridges, large seamounts, or aggregates of smaller objects like seamount chains for example. Finally, we suggest to use frequency bands that approximately fit the typical dimensions of these classes of topographic objects whose role in earthquake nucleation and rupture propagation/ending are expected to be very different. In addition, we have limited the number of roughness parameters for practical reasons. After comparing many frequency bandwidths, we finally chose to work at three significantly different scales: short wavelengths between 12 and 20 km, intermediate wavelengths between 20 and 80 km and long wavelengths between 80 and 100 km.

2.3.2.4. Selection of the Model Used for Calculation

Even though it is less integrative, we have mentioned above that the average model better fits the "real data," especially when considering narrow frequency bandwidths. In this study, we show the roughness values for the narrow wavelength bands ([12 and 20 km] and [80 and 100 km]) obtained with the average model (equation (6)), while the fractal model is used for estimating the roughness over the larger frequency band at intermediate wavelengths, that is, between 20 and 80 km (equation (5)).

Hereafter, we adopt the following notation:

$$R_{\mathrm{HF}} = R_{\mathrm{SW}} = R_{\Delta\lambda/\mathrm{mean}} \text{ in the range } (12 - 20 \text{ km})$$

$$R_{\mathrm{LF}} = R_{\mathrm{LW}} = R_{\Delta\lambda/\mathrm{mean}} \text{ in the range } (80 - 100 \text{ km})$$

$$R_{\mathrm{IF}} = R_{\mathrm{IW}} = R_{\Delta\lambda/\mathrm{fractal}} \text{ in the range } (20 - 80 \text{ km})$$

where R_{HF}, R_{LF}, and R_{IF} refer to roughness estimates at high, low, and intermediate frequencies, respectively, and R_{SW}, R_{LW}, and R_{IW} refer to roughness estimates at short, long, and intermediate wavelengths, respectively.

2.3.2.5. Uncertainties and Validity of the Proxy

Assuming that isotropic PSD are valid, the uncertainty on the roughness values can be estimated using the standard deviation of the PSD in the average model (equation 7 in Text S1 in the supporting information). We typically get values of $\sigma_R \approx 100$ m in the 12- to 20-km wavelength bandwidth and ~200 m in the 80- to 100-km bandwidth. Ninety-five percent of these uncertainties remain below 250 and 450 m for the 12- to 20-km and 80- to 100-km bandwidths, respectively.

More relevant is the applicability of using the seafloor roughness seaward of the trench as a proxy of the subduction interface roughness landward of the trench. Ideally, one should compare the roughness seaward and landward of the trench in regions where the morphology of the seismogenic zone is well constrained. Unfortunately, such imagery down to a depth of typically 50 km is not available. We thus statistically explored the roughness anisotropy in all spatial directions or the roughness similarity normal to the trench versus other directions within a distance of 400 km off the trenches.

We have computed the roughness in the same way as described above but for 12 different orientations spanning 360°. For each orientation, the PSD is limited to samples aligned along this orientation (within a few degrees). Then, we estimate the deviation of these 12 anisotropic PSD where high values means that our hypothesis of isotropy is locally likely to be wrong. We found that these deviations have the same order of magnitude as the deviations estimated above at high frequency but slightly higher at low frequency. They generally do not exceed ~250 m at short wavelengths (150 m in average) and 900 m at long wavelengths (400 m in average). Indeed, as expected, this deviation may be much higher for a few specific regions made of major oriented topography (for example, the Louisville seamount chain off Tonga). Typically, in Japan-Kuril trenches, 15% of the studied area exhibit a clear oriented structure, as the Joban seamount chains or the fracture zone south of it at both wavelengths or the southern trench-parallel bending-related normal faults at high frequency (Figure S1 in the supporting information).

We have also computed the similarity of the roughness spatial distribution pattern when estimated either close to the trench or ~200 km seaward further. To do so, we have divided the 400-km-wide studied strip into two 200-km-wide trench-parallel strips, one closest to the trench and the other seaward. Then, every 1° along all subduction zones, we select a 200-km-along-trench-wide zone on each strip (centered on the node of analysis) and perform a correlation between these two roughness spatial distributions weighted by the total roughness energy. This latter normalization makes the correlation sensitive to the similarity of roughness spatial distribution regardless of the global amplitude. Nevertheless, similar results are obtained with nonnormalized correlation. Such an analysis provides both a quantification of the similarity of the roughness estimation perpendicular to the trench and an indication of a possible better correlation following an oblique direction (see Figure S2 in the supporting information). By doing so, we estimate the degree of similarity between both 200-km-wide strips and validate our proxy concept. The test shows that (1) in most cases the correlation is actually the best in a direction normal to the trench, (2) the fit in normalized-roughness spatial distribution exceeds 80%, and (3) surprisingly it is slightly better for R_{SW} than R_{LW} except for the Sunda trench. To sum up, the roughness of the seafloor prior to subduction appears to be mainly isotropic and displays, statistically, a better similarity in shape with surrounding strips in the trench normal direction.

Mass transfers occurring in the shallow part of the subduction interface, such as sediment offscraping or upper plate removal by subduction accretion (Lallemand et al., 1994; von Huene & Scholl, 1991), may alter the interplate roughness as estimated before subduction. However, numerous observations indicate that the roughness still persists despite the various subduction regimes. This is attested for example by the scars left by the subducting seamounts in the forearc in the Nankai or Hikurangi Troughs or Costa-Rica trench (Kodaira et al., 2000; Pedley et al., 2010; von Huene et al., 2004) or by the observation of subducting seamounts revealed by detailed seismic imagery like beneath the Ecuadorian margin (Collot et al., 2017; Marcaillou et al., 2016) or even at greater depths like beneath the Sumatran margin (Singh et al., 2011). Wang and Bilek (2014) detailed how the subducting seafloor roughness and sediment thickness are important in the seismogenesis. It has also been proposed that the directivity in the tremor sources along the Nankai seismogenic interface were guided by striations at the bottom of the upper plate resulting from paleo-seamounts underthrusting (Ide, 2010). Therefore, we are confident that the seafloor roughness measured immediately seaward of the trench well represents the one immediately landward, even if significant misfits may locally be observed.

3. Results: “SubRough” Database

3.1. Maps

3.1.1. Discrete Roughness Pattern

The global maps of the discrete distribution of the three roughness estimates R_{SW}, R_{LW}, and R_{IW}, over the entire set of subduction zones, are provided in supporting information (Figures S3 to S5, respectively).

3.1.1.1. Short Wavelength Roughness R_{SW}

R_{SW} mapping (Figure S3) highlights bathymetric gradients at high frequencies. Therefore, 95% of R_{SW} values vary in the range 0–300 m with a mean around 145 m (median ~100 m). It clearly illustrates how heterogeneous the seafloor bathymetry is and why there may be no single rule for a rupture to initiate and propagate along the subduction interface. Some gentle aseismic ridges like Carnegie, Nazca, or Ninety-East are not clearly expressed in the roughness signal because almost all their spectral signatures lie at wavelengths longer than 20 km. Other large features are better highlighted like the Obruchev Rise east of the Emperor-seamount chain, the Iquique Ridge off North Chile, the Oki-Daito Ridge south of Kyushu, the East-Pacific Rise off Mexico, or the Nazca-Pacific spreading center off South Chile. Hence, ridges with similar global pattern may have different structure at small scale. Seamounts as small as the ones belonging to the Kinan seamount chain off southwest Japan, whose mean size is about 20–30 km in diameter and ~1 km in height, clearly appear with $R_{SW} > 250$ m. Most fracture zones are detected along their surface trace in R_{SW} signal but only a few of them, like the Grijalva Fracture zone off Guayaquil Gulf in Ecuador, exhibit a linear trend. Many of them, even the largest ones, like the Luzon-Okinawa Fracture zone south of the Ryukyus, are not discernible, that is, having a nonlinear signature.

3.1.1.2. Long Wavelength Roughness R_{LW}

R_{LW} mapping (Figure S4) provides an image of the long wavelength component of elevation changes. Ninety-five percent of R_{LW} values fall in the range 0–1,500 m with a mean around 485 m (median ~250 m). It is a good indicator for topographic changes at large spatial scale. It highlights the main large features that may segment trenches, such as the Louisville Ridge segmenting the Tonga from the Kermadec trenches, the Palau-Kyushu Ridge between the Nankai Trough and the Ryukyu Trench, the Ogasawara Plateau between the Izu-Bonin Trench and the Mariana Trough, or the Emperor seamount chain between Kamchatka and W-Aleutians Trenches. Some fracture zones marked by a pronounced topography are well defined at these wavelengths such as the Investigator FZ south of Sumatra or the Barracuda FZ east of Guadeloupe. Low R_{LW} regions corresponding to sediment fans off Cascadia or Andaman, for example, immediately appear in this mapping.

3.1.1.3. Intermediate Wavelength Roughness R_{IW}

R_{IW} generally mimics the R_{LW} pattern with a larger amplitude, given the fact that PSD are integrated over a wider wavelength interval. Indeed, roughness amplitudes increase with increasing wavelength but also with enlarged wavelength bandwidths. Ninety-five percent of R_{IW} values vary in the range 0–1,500 m with a mean around 635 m (median ~430 m). Since the fractal approach integrates all wavelengths from 20 to 80 km (Figure S5), it is a good technique for mapping objects of intermediate size, namely, seamounts, seamount aggregates, or spreading ridges. In most cases, R_{IW} follows the trend of short- or long-wavelength roughnesses with a mean amplitude about 30% larger than the one of R_{LW} as a result of larger wavelength bandwidth contributions. This observation strengthens our choice to describe the roughness with only two short and long wavelengths parameters. It should be noted that the roughness signal is necessarily dominated by the largest wavelengths up to 80 km. In a few cases, some oceanic features are better defined at intermediate than at short or long wavelengths. R_{IW} mapping brings complementary information with respect to R_{SW} and R_{LW} along the Aleutian, Cascadia, and Ryukyu trenches, for example.

3.1.2. Mean Roughness Pattern

In addition to the discrete data set over a 10-km spatial grid, it may be useful to have access to mean roughness values along trenches for first-order roughness evaluation and correlation with other subduction parameters (see section 4). We have thus averaged the roughness values over a 250 × 250-km^2 area facing each trench node issued from Heuret et al.'s (2011) database, that is, every ~200 km along the trench. Figure S6 (in the supporting information) shows the results in two map views for R_{SW} and R_{LW}. Averaged values are available online in the SubMap database (http://www.submap.fr).

3.2. Global Analysis of Roughness Information Along the Main Subduction Zones

In this section, we examine the lateral variations of R_{SW}, R_{IW}, and R_{LW} with respect to the relative (residual) bathymetry, at middistance between the trench and the seaward boundary of the 250-km-wide strip (i.e., 135 km from the trench, by averaging data along a 2-km-wide band, see Figure 2). Since the general trend of R_{IW} and R_{LW} signals is often the same, except for a few small offsets in their respective peaks, we will not describe R_{IW} to rather focus on R_{SW} and R_{LW}. It should be taken into account that roughness values, even if plotted along a transect, were acquired in a spatial domain within a 100-km-radius sampling circle, so that there could be significant differences between the relative (residual) bathymetry sampled along a 2-km-wide band far from the trench and the roughness peaks and lows sampled over a 200-km-wide area.

3.2.1. Definition of Roughness Classes to Characterize Subduction Segments

Most subduction zones exhibit lateral variations in terms of subducting seafloor roughness. We have thus decided to first characterize the seafloor prior to subduction segment by segment. We have defined our segmentation by taking into account only the 250-km-wide strip close to the trenches in order to optimize the proxy with the subduction plate interfaces. Since we observe a great dispersion of the R_{SW} data and a better coherence for R_{LW}, we have identified seafloor segments based on R_{LW} characteristics only. We define segments larger than 400 km (along-strike), long enough to generate $M_w > 8.5$ earthquakes, except at trench edges where shorter segments may be considered. We then define three classes depending on the percentage of R_{LW} amplitudes less than 250 m and the percentage exceeding 1,000 m (see arrows in Figure 4):

1. the "rough" segments that exhibit a significant proportion of $R_{LW} > 1{,}000$ m (from 14% up to 77%) as well as a limited proportion of $R_{LW} < 250$ m (less than 27%);
2. the "smooth" segments characterized by more than 58% of $R_{LW} < 250$ m (up to 100%) and less than 5% of $R_{LW} > 1000$ m;
3. the "moderately rough" segments are intermediate and do not verify the above criteria except one short segment seaward of the Izu-Bonin Trench, which matches the "smooth" criteria but whose mode (200 km) better fits the moderately rough class (see Figure 4).

The R_{LW} histograms of all segments are plotted in Figure 4 with the mean histogram obtained for each class in bold. Peak values of R_{LW} for each class are respectively 80, 210, and 370 m for smooth, moderately rough, and rough. Standard deviation increases drastically from smooth to rough. We validate a posteriori the two roughness thresholds 250 and 1,000 m used to define the three roughness classes (blue arrows in Figure 4). The R_{SW} histograms (see insert within Figure 4) are more scattered but globally follow the same trend as R_{LW}.

Figure 5 illustrates the respective segment lengths and classes along most subduction zones. We did not perform any statistics for the Mediterranean region as well as along some narrow subduction zones in Southeast Asia, because the length of the segments is too short either because the subduction zones themselves were too narrow or because continents were involved in the subduction.

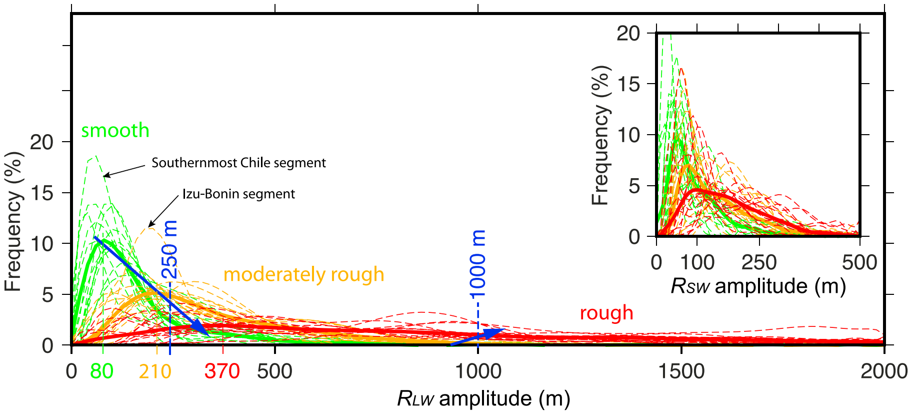

Figure 4. Histograms of R_{SW} and R_{LW} for the three main classes of subducting seafloor. Each dashed line represents a trench segment. The plain lines are synthetic distribution averaging the roughness distributions of all segments within a class. The data set used for the statistics considers the 250-km-wide strip close to the trench. Note that the histograms dispersion within the same class is low for R_{LW} and high for R_{SW}. The blue arrows illustrate the change in roughness distribution from the smoothest class to the roughest.

Table 1 provides a quantitative description of most subduction zones as a function of the different classes of seafloor segments (Figure 5). From the respective contribution of each class, we propose a classification of subduction zones within three groups, spanning from "dominantly rough" (Solomons or Makran) to "dominantly smooth" (Andes or Cascadia). We classify the subduction zones facing moderately rough segments (South Sandwich) or showing strong lateral variations (Izu-Bonin-Mariana [IBM]-Japan-Kamchatka or Luzon) in the "mixed" group.

Typical examples selected among each group are presented in Figures 6 and 7. All other subduction zones are displayed in the supporting information (Figures S7 to S12).

3.2.2. Dominantly Rough Subduction Zones

These trenches are dominated by prominent unsubducted oceanic features, if not already subducting, with more than 14% of $R_{LW} > 1{,}000$ m. We have systematically masked the subducting continental seafloor, as well as areas above sea level from the roughness data set in regions like in the Solomons because we consider that collision processes are out of the scope of our study.

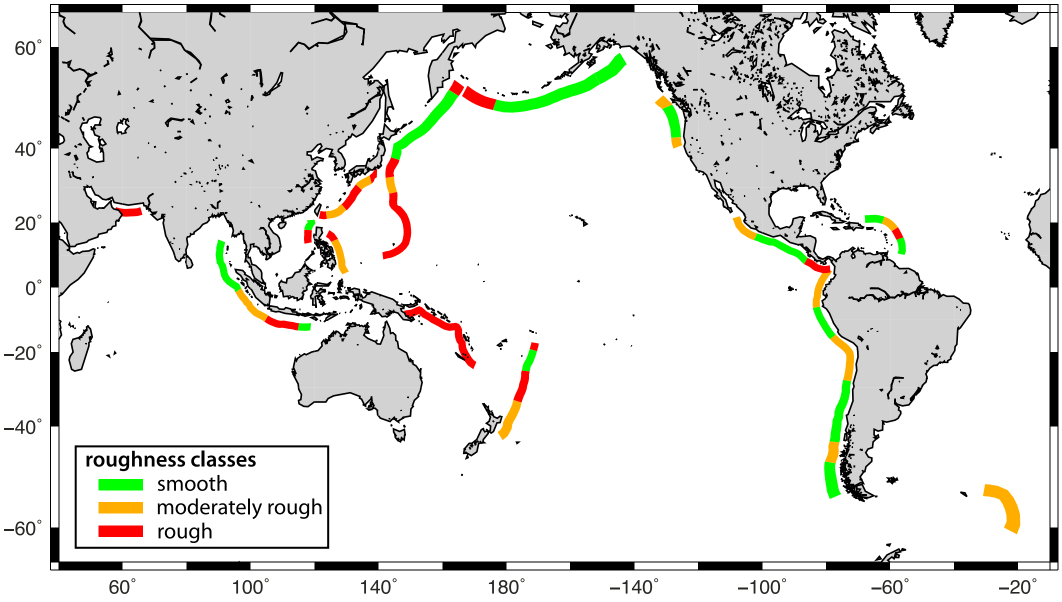

Figure 5. Plot of the seafloor segments seaward of most subduction zones, according to their roughness class.

Table 1
Roughness Types of Oceanic Seafloor Prior to Subduction Along Major Trenches

		Classes		
		Smooth	Moderately rough	Rough
Groups	Trenches	(%)	(%)	(%)
Dominantly rough	Solomons	0	0	100
	Makran	0	0	100
	Ryukyus-Nankai	0	46	54
Mixed	Tonga-Kermadec	23	35	42
	Philippines	0	79	21
	South Sandwich	0	100	0
	Luzon	46	0	54
	Java-Sumatra-Andaman	47	28	25
	IBM-Japan-Kamchatka	48	8	44
Dominantly smooth	Antilles	55	24	21
	Central America	51	25	24
	Aleutians	81	0	19
	Andes	51	49	0
	Cascadia	61	39	0

Note. Classification of the seafloor areas prior to subduction into three groups from the roughest to the smoothest, based on the respective proportion of segments in each class.

3.2.2.1. New Guinea-Solomons-New Hebrides

The Australian plate subducting beneath New Guinea, New Britain, Solomon Islands, and New Hebrides consists in a mosaic of oceanic features including fragments of continental crust as well as oceanic basins, arcs, plateaus, troughs, and spreading centers. This 3,450-km-long subduction zone probably undergoes the rougher morphology among modern subduction systems. Indeed, all roughness parameters reach their highest recorded values there: 46% of the area characterized by $R_{LW} > 1{,}000$ m, 75% with $R_{LW} > 500$ m, and 4% with $R_{LW} < 250$ m. The roughness profile shown in Figure 7a has been masked each time the subducting plate emerges, as at both ends of the subduction system where the Trobriand Platform and the Loyalty Ridge subduct but also in the middle of the trench where the Pocklington Rise and the Rennell Ridge are also subducting. Oceanic basins, that is, Solomon Sea, Woodlark, Santa Cruz, and North Loyalty Basins, exhibit lower roughness values than oceanic reliefs but are still rough with $R_{LW} > 250$ m, except in very restricted areas of the Woodlark and North Loyalty Basins (Figure 6a). Among the various oceanic reliefs, the D'Entrecasteaux Zone—a double-ridge mountain chain—is known to subduct beneath and subsequently causes the uplift of Esperitu Santo Island (Vanuatu; Collot et al., 1985; Fisher et al., 1991).

3.2.2.2. Makran

The Oman Sea seafloor subducting at the 850-km-long Makran Trench shares the same characteristics as the seafloor off the Solomons. The Oman region to the west and the Owen Fracture Zone to the east are major subducting features responsible for 43% of $R_{LW} > 1{,}000$ m. However, the triangular shaped Oman Basin (Figure S7), which is quite narrow at a distance of 135 km from the trench and widens toward the trench, shows very low R_{LW} values.

3.2.2.3. Ryukyus-Nankai

The Philippine Sea Plate subducts along its northwestern side along the 2,300-km-long Ryukyu and Nankai Trenches. Both the northern end of the Luzon volcanic arc colliding with the Taiwan orogen and the Gagua Ridge—a former fracture zone (Deschamps et al., 1998)—contribute to the very high level of both R_{SW} and R_{LW} (77% of $R_{LW} > 1{,}000$ m; see Figure S7 and rough termination in Figure 5). The Amami-Daito-Oki-Daito (ADO) region—remnants of a Mesozoic arc complex—is prominent along the residual bathymetry profile and marked by very high values of R_{SW} and R_{LW} (45% of $R_{LW} > 1{,}000$ m, rough segment in Figure 5). South of the ADO region, the complex fabrics of the West Philippine Basin is reflected in the morphology, thanks to the thin sedimentary cover, increasing roughness parameters to significant levels: up to 250 m for R_{SW} and more than 250 m for R_{LW}. This segment is considered as moderately rough. North of the ADO region, the Palau-Kyushu Ridge, a remnant of the proto-IBM arc, marks the transition between the Ryukyu segment where the West Philippine Basin subducts and the Nankai segment off southwest Japan where

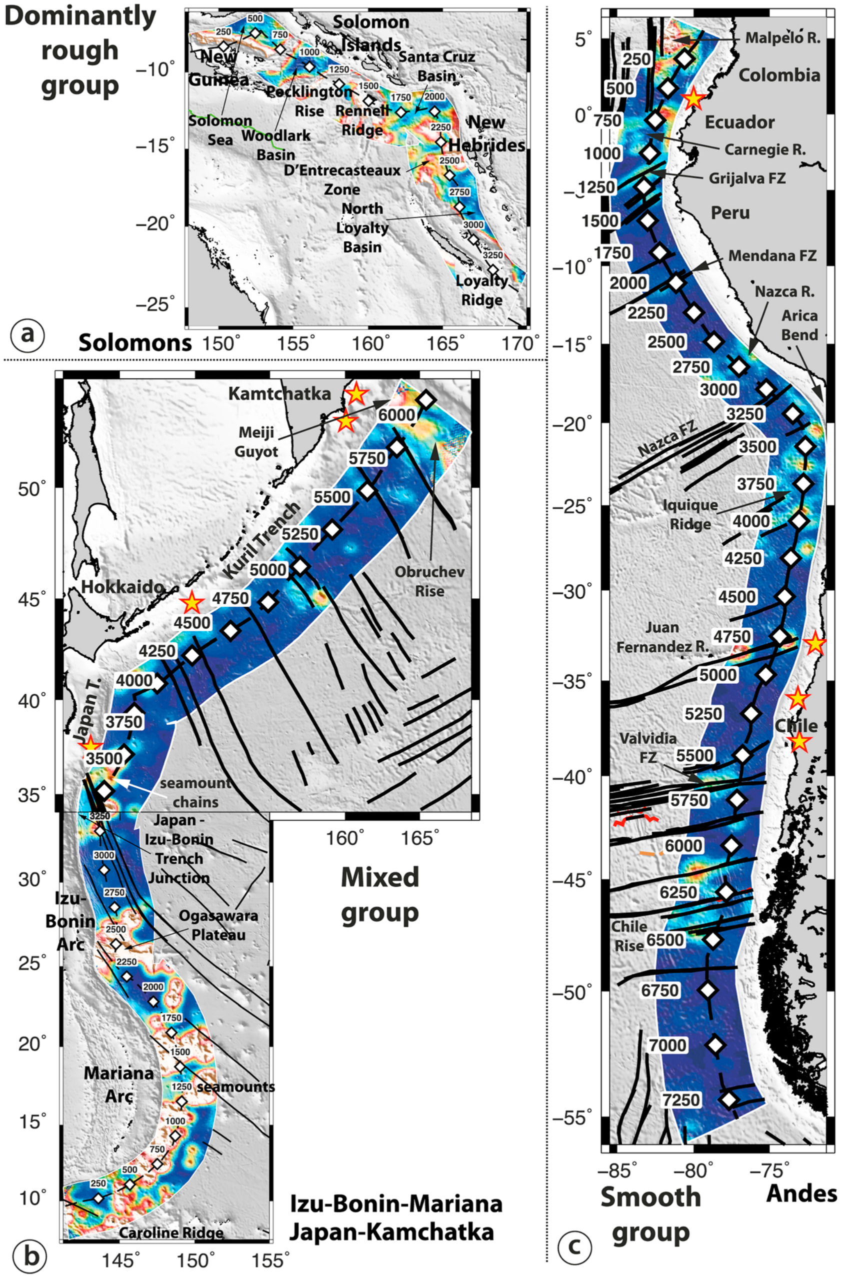

Figure 6. R_{LW} maps representative of the three groups of subduction zones. (a) Dominantly rough group with Solomons, (b) mixed group with Izu-Bonin-Mariana-Japan-Kamchatka, and (c) dominantly smooth group with the Andes all at the same scale. The along-strike profiles of Figure 7, obtained at a distance of 135 km from the trench are plotted as a black dashed line. Diamonds are plotted every 250 km in order to facilitate the comparison with the main features on the profiles.

the Shikoku Basin subducts. This basin, classified as moderately rough (Figure 5), fringes the Nankai Trough. It locally exhibits very low R_{SW} and R_{LW}, despite some intermediate-size seamounts (Koshu and Kinan seamounts) present in its central part (see section 3.3.1 for further details of these seamounts). Several indications of subducting features similar to these seamounts (Kodaira et al., 2000) or extent of the Gagua and Palau-Kyushu Ridges (Dominguez, Lallemand, Malavieille, & Schnürle, 1998; Lallemand, 2016; Park et al., 2009) underneath the margin were reported.

3.2.3. Mixed Subduction Zones

These trenches are characterized by a subducting seafloor either moderately rough or showing lateral variations, that is, rough segments adjacent to smooth or moderately rough ones.

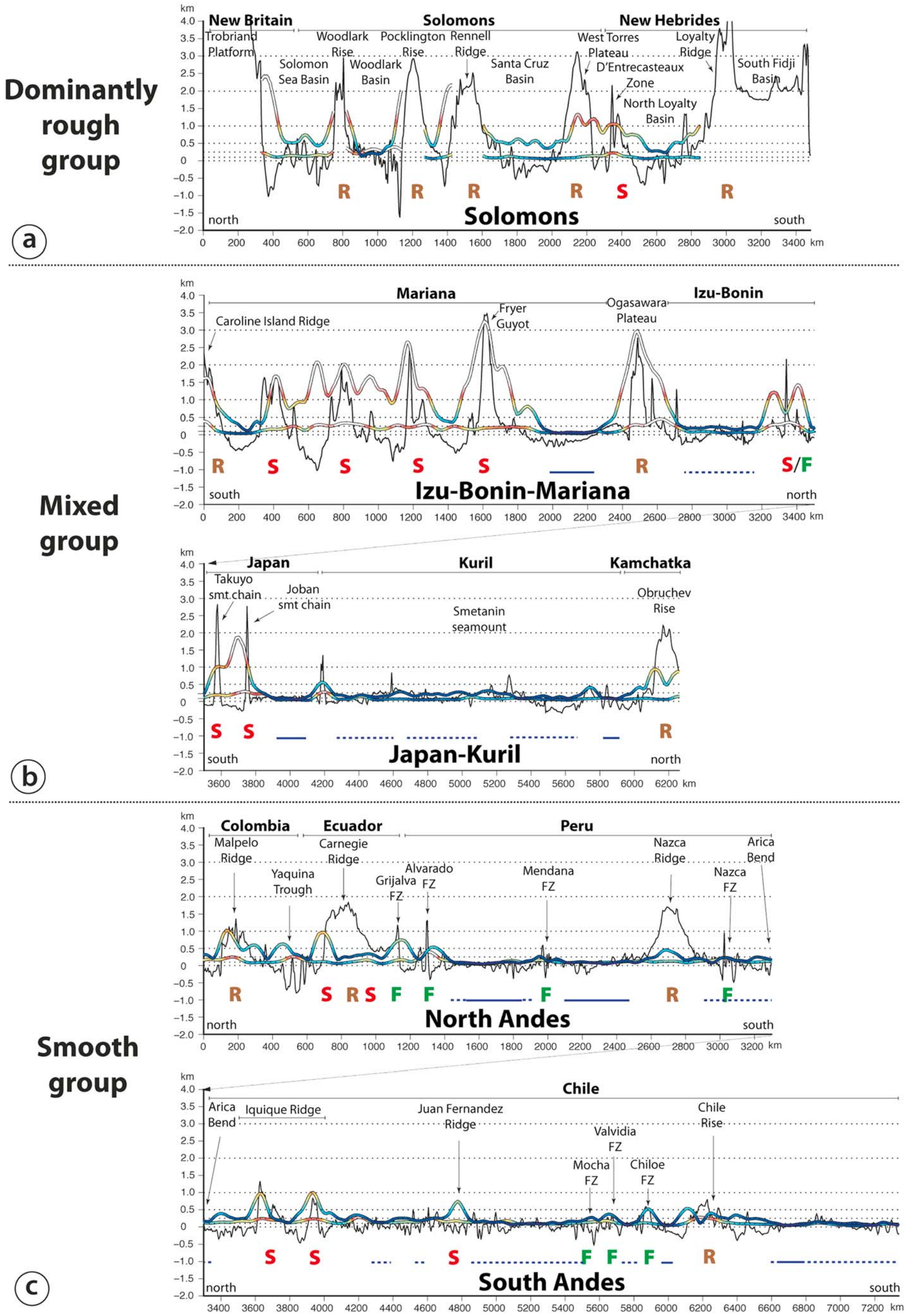

Figure 7. Along-strike profiles of representative subduction zones for each group appearing in Figure 6. Profiles show the relative bathymetry (black line), acquired at a distance of 135 km seaward of the trench (see Figure 2) and associated R_{SW} and R_{LW}. Thin horizontal dotted lines are rulers at 0, 100, 250, 500, 1,000, 2,000, and 3,000 m. S = location of major seamounts or seamount chains or seamount massifs. R = location of major aseismic or active ridges. F = location of major fracture zones. Continuous dark blue lines below the profiles indicates the very smooth regions characterized by R_{SW} and $R_{LW} < 100$ m. The dotted dark blue lines outline areas with moderately smooth seafloor, for example, R_{SW} and $R_{LW} < 250$ m.

3.2.3.1. IBM-Japan-Kamchatka

Typically, this 6,250-km-long subduction zone is composed of a southern rough part where the old Mesozoic Pacific seafloor subducts along the 3,500-km-long IBM Trench and a northern, essentially smooth, part extending from northern Japan, through the Kurils to the Kamchatka (Figure 6b).

The Caroline Ridge and the Ogasawara Plateau, both characterized by $R_{LW} > 1{,}000$ m, are major features that control the Mariana Trench shape at both south and north terminations (e.g., Wallace et al., 2009). Numerous seamounts, scattered all along this trench segment, boost the roughness values around 250 m for R_{SW} and above 1,000 m for R_{LW}. Low roughnesses ($R_{\mathrm{SW}} < 100$ m and $R_{\mathrm{LW}} < 250$ m) are also observed over a few hundreds of kilometers on both sides of the Ogasawara Plateau (Figures 6b and 7b). As mentioned in section 3.2.1, the 480-km-long segment north of the Ogasawara Plateau (Figure 5) has been classified as moderately rough because of its R_{LW} mode around 200 m, even if it also fits the smooth class criteria (73% of $R_{\mathrm{LW}} < 250$ m, Figure 4).

Most of the Lower Cretaceous Pacific seafloor, subducting beneath Kuril and northern Japan island arcs, presents a rather smooth, moderately hilly morphology characterized by $R_{\mathrm{SW}} \approx 100$ m and 65% of $R_{\mathrm{LW}} < 250$ m (mode ≈ 110 m) over almost 2,000 km compared with the total length of the Japan-Kuril-Kamchatka Trench: 2,750 km. The lowest R_{LW} values are recorded off Tohoku, northern Honshu. Both R_{SW} and R_{LW} increase significantly, up to 300 and 2,000 m, respectively, south of the Japan Trench where the Joban and Takuyo seamount chains obliquely intersect the trench (Figure 7b). The extension of the seamount chain beneath the Japan margin has been demonstrated by seismic imaging (Lallemand et al., 1989; Mochizuki et al., 2008). Near the northern termination off Kamchatka, R_{LW} increases up to 1,000 m over the Meiji Guyot and Obruchev Rise, which belong to the Hawaii-Emperor hotspot seamount chain.

3.2.3.2. Tonga-Kermadec

The 3,400-km-long Tonga-Kermadec subduction system (Figure S8) is segmented at the latitude of the Louisville hotspot chain, which consists in a seamount chain associated with R_{SW} up to 250 m and R_{LW} up to 2,900 m. North of its intersection with the trench, the Pacific seafloor off the Tonga archipelago, even significantly offset by bending-along-strike-normal faults, exhibits rather low roughness values (78% of $R_{\mathrm{LW}} < 250$ m with a mode of ~70 m along the 720-km-long smooth segment), except at the two extremities where huge seamounts (Capricorne and Osbourn seamounts) enter the trench (Figure 5). The Louisville Ridge has been detected, up to 60-km arcward from the trench, beneath the Tonga margin based on residual bathymetry by Bassett and Watts (2015a). It is known to have severely damaged the Tonga Trench during its southward creeping (Lallemand et al., 1992; Pelletier & Dupont, 1990).

The seafloor off the Kermadec Islands, south of Louisville seamount chain, is characterized by elongated seamounts and ridges producing high amplitudes of R_{SW}, up to 250 m, and R_{LW}, up to 1,200 m (Figure S8). A sharp step is crossed near 36°S coinciding with the northern limit (scarp) of the Hikurangi Plateau. Despite its elevation above the abyssal plain, the plateau is rather flat with several scattered seamounts on top increasing the level of roughness ($R_{\mathrm{SW}} < 100$ m, $R_{\mathrm{LW}} < 500$ m). Some of them have profoundly damaged the Hikurangi margin (Collot et al., 2001; Lewis et al., 1998, 2004; Pedley et al., 2010). These subducting seamounts may explain the dominant creeping behavior along the Higurangi subduction interface according to Gao and Wang (2014). At the southern end, the profile abuts against the E-W-trending shallow Chatham Rise.

3.2.3.3. Philippines

The West Philippine Basin Eocene oceanic crust subducts beneath the Philippine archipelago along the 1,550-km-long Philippine Trench. The middle subducting segment facing South Leyte and North Mindanao Islands is moderately rough with $R_{\mathrm{SW}} < 100$ m and 34% of $R_{\mathrm{LW}} < 250$ m (Figure S9). The southern part of the subducting seafloor (Palau Basin) is locally rougher when crossing the Mindanao Fault but still classifies as moderately rough.

The seafloor becomes rougher in the north as the result of ridge-plume interaction in Eocene (Deschamps & Lallemand, 2002; Ishizuka et al., 2013) with R_{LW} up to 2,000 m where the Benham Rise intersects the trench.

3.2.3.4. South Sandwich

The South America oceanic crust subducts along the 1,200-km-long South Sandwich trench (Figure S9). Despite numerous fracture zones branched onto the close South America-Antarctica spreading center, roughness parameters never exceed 400 m for R_{LW} (except at the northern extremity approaching the South Georgia Rise) and 300 m for R_{SW}. With 54% of $R_{\mathrm{LW}} < 250$ m and only 1% of $R_{\mathrm{LW}} > 1{,}000$ m, it is close to belong to the smooth class, but we still classified it as moderately rough (Figure 5; Table 1).

3.2.3.5. Luzon

The Chinese Platform subducts beneath Taiwan along the northernmost part of the 1,200-km-long Luzon Trough (Figure S9). We did not process the northern part where continental crust collides with the Luzon volcanic arc.

South of the continental talus, where the South China Sea oceanic seafloor subducts, we observe that the northern part, supplied by sediments coming from Taiwan, is very smooth with both R_{SW} and $R_{LW} < 100$ m (75% of $R_{LW} < 250$ m), while the southern part off Luzon Island is extremely rough. The high roughness values (R_{SW} up to 300 m and R_{LW} up to 2,500 m); 26% of $R_{LW} > 1{,}000$ m) are associated with the subducting Scarborough seamount chain, which aligns along the N80°-trending fossil spreading center. Wang and Bilek (2014) discussed the roughness of the igneous crust, almost concealed by the sediment cover in the north "smooth" part, considering that once most of the sediment cover offscraped at the front of the upper plate, the subducting seafloor may become rugged and promote creeping along the subduction interface.

3.2.3.6. Andaman-Sumatra-Java-Sumba

As the IBM-Japan-Kamchatka subduction zone, the seafloor facing the 5,100-km-long Andaman-Sumatra-Java-Sumba subduction zone is segmented into smooth segments off Andaman Islands and between Java and Sumba islands, and rougher ones especially south of Java (Figure S10).

The morphology is extremely smooth off Andaman Islands and northern Sumatra laterally over about 1,000 km of seafloor with both R_{SW} and $R_{LW} < 100$ m, mainly as the result of high sediment supply from the Bengal fan (70% of $R_{LW} < 250$ m, R_{LW} mode ≈ 40 m). Only the N-S-trending Ninety-East Ridge overhangs the abyssal plain at a distance from the trench with R_{LW} up to 800 m, fringing the trench without being subducted yet (Moeremans & Singh, 2014).

To the south, off central and southern Sumatra, numerous north-south trending fracture zone reliefs, like the 97°E or the Investigator fracture zones, contribute to higher roughness amplitudes especially at long wavelengths as the oceanic sedimentary cover becomes thinner (29% of $R_{LW} < 250$ m, 33% of $R_{LW} > 500$ m). Similar roughness patterns have been observed from seismic reflection and gravity data in the seismogenic zone beneath the margin (Henstock et al., 2016). This segment has been classified as moderately rough (Figure 5).

The 1,140-km-long southern segment of the Sunda Trench, off Java, is characterized by a rough subducting seafloor. We distinguish from west to east the Christmas Island, the Roo Rise, and the Australian Rise, all associated with 25% of $R_{LW} > 1{,}000$ m (Figures 5 and S10). Surprisingly, most of the R_{SW} values do not exceed 100 m, whereas only 8% of $R_{LW} < 250$ m, attesting that oceanic features wavelengths are larger than 20 km wide. The 440-km-long easternmost segment, abutting against the Australian Rise, presents smooth characteristics with 58% of $R_{LW} < 250$ m.

3.2.4. Dominantly Smooth Subduction Zones

This group of trenches exhibits more than 58% of $R_{LW} < 250$ m together with a maximum of 5% of $R_{LW} > 1{,}000$ m (Figure 4 and Table 1).

3.2.4.1. Andes

The 7,350-km-long Andean Trench (Figure 6c) shows strong lateral variations in the morphology of the subducting seafloor alternating moderately rough segments with longer smooth ones. In Figure 7c, we have divided this long subduction system into two segments on both sides of the Arica bend: a North Andes segment 3,300 km long and a South Andes segment 4,050 km long.

Starting from the north, off Colombia, Ecuador, and northernmost Peru, the Nazca Cenozoic seafloor is very irregular with plume-derived ridges (Malpelo and Carnegie), trough (Yaquina T.), and fracture zones (e.g., Grijalva, Alvarado, and Sarmiento ridges) producing moderately high roughness values (22% of $R_{LW} < 250$ m, 4% of $R_{LW} > 1{,}000$ m). Off the Peru Trench, the seafloor is smoother (95% of $R_{LW} < 250$ m) with both R_{SW} and $R_{LW} \approx 100$ m except across the sharp Mendaña and Nazca fracture zones ($R_{LW} \approx 250$ m) and the 300-km-wide Nazca Ridge ($R_{LW} \approx 500$ m). Interestingly, the two main aseismic ridges, that is, Carnegie and Nazca, culminating at about 1,600 m above the surrounding seafloor, have a relatively small roughness signature, especially at short wavelengths. These major features are known to extend beneath the margin as well as volcanic massifs on the flanks of the Carnegie Ridge observed on both sides of the trench (Collot et al., 2017; Gutscher et al., 1999, 2000; Marcaillou et al., 2016).

South of the Arica bend, the Nazca seafloor becomes locally rougher with several scattered seamounts on both sides of the Iquique Ridge, showing values comparable to those in the northernmost Andes (R_{SW} up to 250 m, 33% of $R_{LW} < 250$ m, and R_{LW} up to 1,000 m). Similar seamounts were detected, based on multichannel seismics imagery, into the subduction channel landward of the trench. They are suspected to have controlled interplate coupling and seismic rupture in the 2014 Iquique earthquake area (Geersen et al., 2015). South of this moderately rough area and over 1,780 km, the seafloor shows short wavelengths oceanic fabric (R_{SW} and 82% of $R_{LW} < 250$ m) sometimes punctuated by the Juan Fernandez seamount chain (R_{LW} up to 700 m). Then, the moderately rough segment of the Chile Rise and young fracture zones (i.e., Mocha, Valvidia, and Chiloe) boosts the roughness values up to 500 m for long wavelengths and 250 m for short wavelengths (41% of $R_{LW} < 250$ m). The continuation of those features, as well as the variable thickness of the subduction channel, beneath the Chile margin has been investigated by Contreras-Reyes et al. (2010). They have noted a probable tectonic control of the 1960 and 2010 Chiloe and Maule giant earthquakes. South of the trench-trench-ridge triple junction, the Antarctica seafloor smooths again drastically over 770 km showing the lowest roughness values of the Andean Trench near 100 m for both R_{SW} and R_{LW} (100% of $R_{LW} < 250$ m). Finally, the seafloor along the Chile trench is probably one of the most extended (total of 3,730 km long) smooth subducting seafloor in the world.

3.2.4.2. Antilles

The Cretaceous Atlantic seafloor is subducting beneath the Caribbean Plate from Hispaniola Island to Trinidad along the 2,200-km-long Puerto Rico and Lesser Antilles trenches (Figure S11). Similarly with the Tonga Trench where strong plate bending does not increase roughness, we observe a smooth seafloor along the 560-km-long segment north of Puerto Rico, characterized by extremely low roughness values (both R_{SW} and $R_{LW} < 100$ m, 69% of $R_{LW} < 250$ m). Then, R_{LW} increases off Saint Martin, Antigua, and Barbuda (500-km-long moderately rough segment, 34% of $R_{LW} < 250$ m), reaching a maximum of 1,200 m off Guadeloupe where fracture zone ridges like Barracuda and Tiburon intersect the trench (360-km-long rough segment, 13% of $R_{LW} < 250$ m and 21% of $R_{LW} > 1{,}000$ m). Those ridges extend far beneath the Lesser Antilles accretionary wedge and arc basement, as seen on seismic reflection profiles (Laigle et al., 2013). The seafloor smoothens again off Barbados Island in the south, partly as a consequence of the Orinoco sediment supply, with extremely low roughness values similar to those off Puerto Rico (600-km-long smooth segment, 69% of $R_{LW} < 250$ m). R_{LW} increases at the southern end near the Demerara Plateau and at the northern end at the vicinity of the Bahamas Bank.

3.2.4.3. Central America

The Neogene Cocos Plate, subducting beneath Central America along the 3,450-km-long Middle America Trench, is limited to the north by the East Pacific Rise and highly tectonized young seafloor (Rivera fracture zone and massif), and to the south by the Cocos Ridge originating from the Galapagos hotspot, and the Panama fracture zone (Figure S11). The seafloor facing Central America has been divided into three segments (Figure 5).

The 970-km-long northern segment is moderately rough with 34% of $R_{LW} < 250$ m, up to 1,200 m near the Rivera Massif. The main middle segment, 1,930 km long, is globally smooth with 88% of $R_{LW} < 250$ m, up to 600 m close to the Tehuantepec Ridge, a major fracture zone branched onto the East Pacific Rise. North of that ridge, R_{SW} maintains a high level up to 250 m north (Figure S11). The smoothest section, about 1,100 km wide with $R_{SW} < 100$ m and $R_{LW} < 250$ m, is observed south of the Tehuantepec Ridge off Guatemala, El Salvador, Nicaragua, and northern Costa Rica. Northwest of the Cocos Ridge, offshore Costa Rica, several scattered conical seamounts are observed seaward and landward of the trench. They produce embayments in the small accretionary wedge and remarkable scars into the forearc as they subduct far from the trench (Dominguez, Lallemand, Malavieille, & von Huene, 1998; Dominguez et al., 2000; Ranero & von Huene, 2000; von Huene et al., 1995, 2000). The 980-km-long southernmost segment includes the Cocos Ridge and the Panama fracture zone. We consider it as a rough segment characterized by 18% of $R_{LW} > 1{,}000$ m and 12% of $R_{LW} < 250$ m.

3.2.4.4. Aleutians-Alaska

The Pacific seafloor, which subducts beneath the 3,750-km-long Aleutians-Alaska Trench, is globally smooth except in its western portion (Figure S12). This 730-km-long westernmost segment coincides with the northern termination of the Hawaii-Emperor seamount chain at the junction between the Kamchatka and Aleutian trenches. There, the seafloor is very irregular including the Detroit Tablemount, the SW Aleutian and the Aleutian Rises. R_{LW} reaches values as high as to 1,300 m whereas R_{SW} may exceed 250 m along this rough segment (15% of $R_{LW} > 1{,}000$ m and 14% of $R_{LW} < 250$ m).

The rest of the seafloor subducting to the east over more than 3,000 km maintains a high level of R_{SW} up to 250 m, while R_{LW} decreases below 500 m due to the presence of several N-S-trending fracture zones (Rat and Amlia for example). The lowest roughness values are measured off the Eastern Aleutians and the Western Alaska Peninsula. Only the Sirius seamount, south of Shumagin margin, interrupts the low roughness level ($R_{\mathrm{LW}} < 250$ m) of this ~1,400-km-wide area. Both R_{SW} and R_{LW} increase again south of Kodiak Island in response to the presence of the Patton and Giacomini seamounts. This long segment is undoubtedly smooth as it shows 85% of $R_{\mathrm{LW}} < 250$ m (Figure 5).

3.2.4.5. Cascadia

The 400-km-wide central part of the very young Juan de Fuca Plate subducting beneath British Columbia, Washington, and Oregon states is extremely flat, as it is filled by the large Nitinat and Willapa sediment fans. R_{SW} and R_{LW} values are very low (<100 m) compared with those on both northern and southern segments of this 1,200-km-long subduction zone. Indeed, the oceanic fabric, including a spreading center and fracture zones (e.g., Mendocino and Sovanco FZ with R_{SW} up to 500 m) covered with fewer sediment, explains the irregular seafloor morphology there. Interestingly, R_{SW} exceeds R_{LW} in amplitude over some oceanic features like the Explorer and Juan de Fuca Ridges, the Blanco, and the Mendocino Fracture Zones. We classified the 780-km-long middle segment as extremely smooth (98% of $R_{\mathrm{LW}} < 250$ m) and the two short (250 km long each) edge segments as moderately rough (48% of $R_{\mathrm{LW}} < 250$ m).

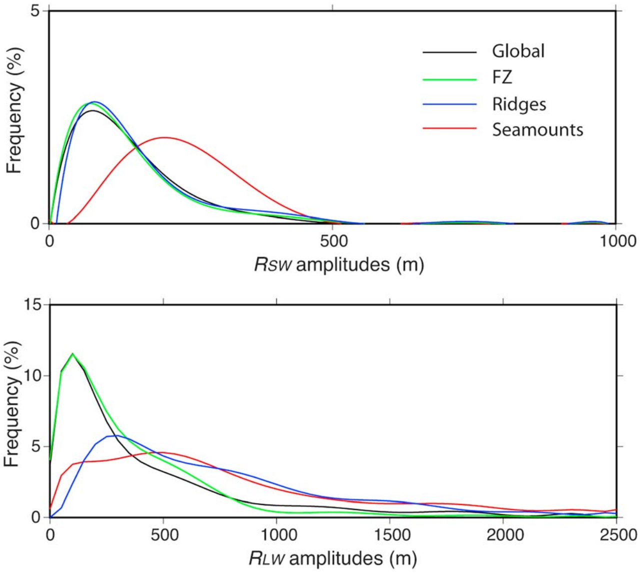

Figure 8. Distribution of roughness values among the global data set (in black) or subdata sets (in color) corresponding to major oceanic features.

3.3. The Roughness of Oceanic Features

Main categories of oceanic features such as seamounts, ridges, or fracture zones are noted along profiles in Figures 7 and S8 to S12 as S, R, and F, respectively. Those features are known for contributing to the seismogenic behavior along the subduction interface. Here we will examine their roughness signature before subduction with respect to the global roughness pattern (Figure 8 and Table 2).

3.3.1. Seamounts, Seamount Massifs, and Seamount Chains

Seamount are extremely abundant on oceanic plates. They cover a great variety of morphological aspects. They are often isolated with various sizes and shapes. Eighty-three percent of detected seamounts are less than 3 km high, more or less conical, sometimes truncated. Those higher than 3 km are generally reshaped by rift zones, flank collapses, subaerial erosion by the waves or reef development (Dominguez, Lallemand, Malavieille, & von Huene, 1998; Kim & Wessel, 2011; Wessel, 2001). Figure 8 shows the R_{SW} and R_{LW} pattern over seamounts with respect to the global roughness pattern. We have analyzed all roughness values from the 10-km-spaced grid inside the seamount contours as defined by Kim and Wessel (2011) within the 250-km-wide strip along the trenches. As expected, the mean roughness is higher than the global trend (mean R_{SW} = 234 m instead of 144 m; mean R_{LW} = 909 m instead of 490 m; mean R_{IW} = 1,380 m instead of 634 m; see Table 2). However, it appears that the difference from the global trend is particularly clear when looking at short wavelengths on the density plot in Figure 8. Seamounts also appear as aggregates or massifs as the Rivera Massif off Mexico, the Atacames seamounts, for example, on the northern flank of the Carnegie Ridge (Marcaillou et al., 2016), or chains like the Koshu or Kinan seamount chains south of the Nankai Trough, the Joban seamount chain subducting in the Japan Trench, or the Iquique Ridge off north Chile (Figures 6, 7, S7, and S11). In those cases, the seamount size is typically 2 to 3 km high and 15 to 50 km in diameter. Their roughness signal ranges from 200 to 300 m for R_{SW} and from 400 to 2,000 m for R_{LW}. The long wavelength roughness amplitude is sensitive, not only to the seamount morphology itself but also to the surrounding morphology over a wider area.

Many ridges like the Louisville Ridge, the Juan Fernandez Ridge, the D'Entrecasteaux Zone, or the Kashima seamount chain, are composed of aligned large-size seamounts either originating from hotspots or controlled by major faults (Figures 6, 7, and S8). Their signature is then anisotropic as any seamount chain like

Table 2
Mean Roughness Amplitudes of Specific Oceanic Features Compared with Global Trend

	R_{SW} amplitude (m)			R_{LW} amplitude (m)			R_{IW} amplitude (m)		
	Mean	Median	σ_R	Mean	Median	σ_R	Mean	Median	σ_R
Global	144	119	100	490	287	544	634	429	627
Fracture zones	141	115	99	394	275	379	625	423	625
Ridges/plateaus	163	121	119	835	652	664	845	652	678
Seamounts	234	232	95	909	665	767	1,380	1,155	863

Note. Mean roughness values and standard deviation (in meters) applied for the global database and for specific morphological features.

the Scarborough seamount chain off Luzon or the Joban seamount chain. Seamounts taller than 3 km have a strong signal especially on R_{LW}.

3.3.2. Fracture Zones

Fracture zones often appear as linear features that can be followed over hundreds or thousands of kilometers. They clearly extend into the subducting slabs and are often supposed to affect the seismic behavior of the plate interface (Carena, 2011; Das & Watts, 2009; Müller & Landgrebe, 2012). Taken all together and investigating an area located 10 km away on each side of the fracture zones, their roughness signal does not differ much from the global seafloor one (Figure 8): mean R_{SW} = 141 m instead of 144 m and mean R_{LW} = 394 m instead of 490 m. In most cases, due to their spatial extent and their low elevation gradients, the fracture zone contribution to roughness is not significantly different from its vicinity. In a few cases, the oceanic crust age contrast, and vertical offset, across the fracture zone are enough to produce a significant difference in elevation, for example, 500 m across the Grijalva FZ off Ecuador or the Mindanao FZ off the Philippines. Such morphological step is marked by R_{LW} = 700–1,000 m (Figures 6, 7, and S9) because this parameter is very sensitive to slope gradients, but such case is very rare. Some fracture zones—generally named ridges—have been the locus of localized deformation and rise, as the Gagua Ridge east of Taiwan, the Owen Fracture Zone off Makran (Figure S7) or the Barracuda Ridge off Lesser Antilles (Figure S11). In those cases, R_{LW} ranges from 1,000 to 2,000 m. The maximum is reached at the Owen FZ because the ridge evolved in a transtensional context and is now bordered by pull-apart basins as the Dalrymple Trough (Rodriguez et al., 2013), increasing the slope gradient.

3.3.3. Aseismic and Active Ridges and Plateaus

Here we consider all elongated prominent features as well as plateaus other than fracture zones or seamount chains. As for seamounts, the mean roughness values of these features are higher than for global seafloor, especially for long wavelengths: mean R_{SW} = 163 m instead of 144 m and mean R_{LW} = 835 m instead of 490 m. The maximum R_{LW} amplitude—typically 600–1,000 m—is generally observed along the flanks of the Hikurangi Plateau, Cocos, Carnegie, Malpelo, Obruchev, or Ninety-East Ridges when their width is larger than 100–200 km (Figures 6, 7, S8, S10, S11, and S12). Narrower features like Palau-Kyushu Ridge, Amami Plateau, Daito Ridge, Pocklington Rise, or SW Aleutian Ridge share similar signals with seamounts, that is, high R_{SW} and R_{LW} (Figures 6, 7, S7, and S12). Active ridges like the Chile, the Juan de Fuca, or the Gorda Rise (Figures 6, 7, and S12) show higher R_{SW} up to 250 m because of the high bathymetric signal frequency but no or few anomalies in R_{LW}.

3.3.4. Smooth Areas

Continuous smooth areas are outlined in Figures 6, 7, and S7 to S12. Plain lines correspond to regions with both R_{SW} and R_{LW} less than 100 m, that is, very smooth regions, whereas dotted lines highlight regions with both R_{SW} and R_{LW} less than 250 m, that is, smooth regions compared with their surroundings. Among the smoothest regions (R_{SW} and $R_{LW} < 100$ m), some reflect a smooth oceanic crust like off the northernmost Mariana arc (250 km of lateral extent), Puerto Rico (150 km), northern Japan (200 km), northern Kuriles (<100 km), Eastern Aleutians (350 km), Peru (400 km on each side of the Mendana FZ), Guatemala (150 km), and Nicaragua (200 km). Other regions are smooth because of an excess of terrigenous sediment filling the trench like Andaman (400 km), northern Sumatra (400 km), Barbados (100 km), Cascadia (300 km), western Alaska (250 km), south Chile (≈100 km on each side of the Chile Rise). Many smooth areas

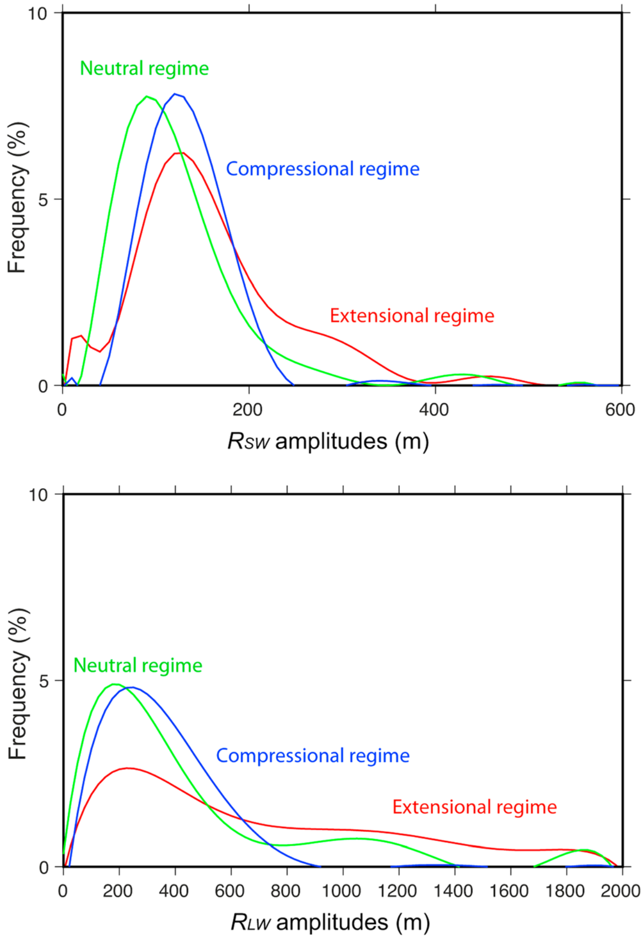

Figure 9. Distribution of roughness values of seafloor facing regions characterized by different upper plate strain regimes as defined by Heuret and Lallemand (2005).

extend laterally with moderately smooth areas (R_{SW} and $R_{\mathrm{LW}} < 250$ m) like off Middle America, southern Chile, Aleutians, or Antilles. The above evaluation of the smooth area extents has been done at a distance of 135 km from the trench. The lateral extent may thus vary in the direction normal to the trench but not drastically since the roughness values are calculated from a 200-km-wide sampling area (see Figure 2).

4. How Does the Seafloor Roughness Correlate With the State of Stress in the Subduction Zones?

This study is the first step to investigate several topics such as the relationship between subduction interface roughness and seismicity but also margin's tectonic behavior. Here we analyze the correlation with subduction parameters, which may be potentially controlled by the roughness of the plate interface. In this respect, we have selected parameters dealing with the state of stress within the converging plates as well as the plate interface to test the influence of the plate boundary topography on it. Thus, we test three proxies of the state of stress in the subduction zone: the upper plate strain at a distance from the plate interface as defined by Heuret and Lallemand (2005), the seismic coupling as estimated by Heuret et al. (2011), and the *b* value as estimated by Nishikawa and Ide (2014).

4.1. Correlation With Upper Plate Strain

We have used the SubMap database (Heuret & Lallemand, 2005, http://www.submap.fr) to extract the upper plate strain along most subduction zone transects. Following Jarrard's (1986) study, Heuret and Lallemand (2005) have estimated the strain regime of oceanic subduction zones in a semiquantitative way based on most representative focal mechanisms of earthquakes occurring within the upper plate at a distance from the trench, that is, in the arc and back-arc domains. In this study, we have reduced the seven initial strain classes from highly extensional (back-arc spreading) to highly compressional (back-arc shortening) into only three strain classes: extensional, neutral, and compressional. The strain classes estimated over 200-km-wide transects have been correlated with 200-km-wide sampled mean roughness parameters obtained along trenches (see section 3.1.2, Figure 9). With respect to neutral regimes, compressional regimes correlate with slightly higher roughness amplitudes. The main difference is observed with extensional regimes that are associated with significantly larger roughness amplitudes especially at long wavelengths.

4.2. Correlation With Seismic Coupling

Seismic coupling coefficients, that is, the ratio of the amount of seismic slip to total amount of plate convergence over about a century (e.g., Peterson & Seno, 1984; Ruff & Kanamori, 1983), should normally range from 0 (pure creep) to 1 (all the slip is seismic). Since it is calculated over a period that could be shorter than the recurrence time of great earthquakes, the seismic coupling coefficient may be larger than 1. We have used the values estimated by Heuret et al. (2011, www.submap.fr) based on Brune (1968) and computed over the period 1900–1975 using the Centenial catalog and 1976–2007 using the Harvard catalog, seismogenic zone dimensions deduced from seismicity analysis (Heuret et al., 2011), and a plate interface rigidity equal to 5×10^{10} N/m^2. The seismic coupling coefficients have been calculated over subduction segments typically 400 to 1,000 km long, whereas the roughness mean values are obtained over a distance of 200 km along trench. For that reason, the same seismic coupling value may be correlated with different mean roughness values.

The cross correlation between both R_{SW} and R_{LW} and seismic coupling is shown in Figure 10. It is noteworthy that high seismic coupling (>0.5) is systematically observed for relatively small roughness amplitudes at both

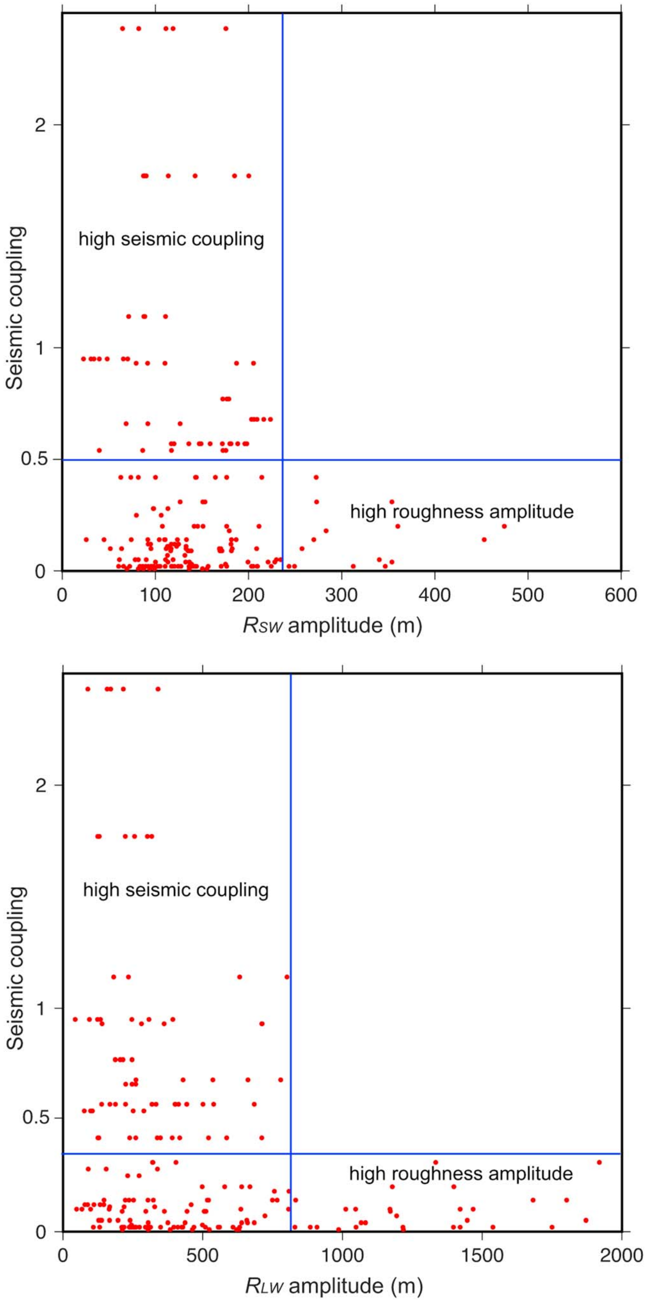

Figure 10. Distribution of roughness values of seafloor facing regions characterized by different seismic coupling coefficients as defined by Heuret et al. (2011).

short and long wavelengths, respectively less than 230 and 800 m. Reversely, relatively high roughness amplitudes ($R_{SW} > 230$ m and $R_{LW} > 800$ m) are systematically associated with low seismic coupling <0.5.

4.3. Correlation With *b* Values

The *b* value, that is, the negative slope of the power law frequency size distribution of earthquakes, is supposed to be correlated with the shear stress (Gutenberg & Richter, 1944): The higher the *b* value, the lower the shear stress. Nishikawa and Ide (2014) have estimated the *b* values in 88 regions, 500-km-along-strike-wide each, where the number of seismic events (at least 100 events), issued from the Advanced National Seismic System catalog from 1978 to 2009, was sufficient to estimate the completeness magnitude. They found a positive relation with the buoyancy of the subducting plate (plate age and trench depth) and no significant relation with the horizontal force balance (convergence rate and upper plate velocity). Among the 88 regions studied by Nishikawa and Ide (2014), we have been able to correlate the *b* values for 70 of them where roughness data were coincident. To be coherent with the sampling area used by the authors to calculate the *b* values, we have analyzed the coincident roughness over a similar trench length within a 250-km-wide strip seaward of the trench. Figure 11 shows that there is no significant correlation between the roughness and the *b* value.

5. Discussion

The sensibility of mega-earthquake rupture propagation to the amplitude and wavelength of the seismogenic subduction interface topography is still unclear. In this study, we have made the choice to focus on roughness rather than residual bathymetry, in order to better account for not only the absolute distribution of the elevation but also for the relative deviation of the elevation around its mean value in a wide range of frequencies. In other words, we put the emphasis not only on the characterization of the subducting features themselves but also on the topography gradient in the vicinity of the subducting features over distances comparable with those of large ruptures. This study provides a complete data set of roughness characteristics along most oceanic subduction zones. Detailed correlations between the discrete distribution of the seafloor roughness and the seismogenic potential of the plate interface focusing on nucleation, propagation, maximum slip, and arrest of the ruptures requires great attention and cannot be treated here. It is the topic of a complementary study (van Rijsingen et al., 2018).

5.1. No Specific Roughness Signature for Fracture Zones

It is somewhat surprising that transform faults and fracture zones do not differ in their roughness signal from the global trend at both short and long wavelengths (Figure 8). Statistically, it means that the distribution of seafloor elevations has similar amplitudes and wavelengths as these linear features. In detail, we have observed that many of them can be traced on roughness maps: Investigator FZ, Ninety-East Ridge, and Grijalva FZ, for example, but in average they do not significantly differ from the background signature. The literature provides contrasting arguments regarding the effect of subducting fracture zones on earthquakes triggering. Müller and Landgrebe (2012) claim that the occurrence of great ($M \geq 8$) subduction earthquakes is strongly biased toward regions associated with intersections of oceanic fracture zones and subduction zones, but they also admit that those characterized by uplifted ridges are more prone to cause strong and persistent coupling in the subduction interface. Robinson et al. (2006) or Das and Watts (2009) saw a clear link between those features and the dynamics of the rupture during large earthquakes like the 1986 M_w8.0 Andreanof Islands event or the 2001 M_w8.4 Peru event. In these cases, the rupture stalled by the fracture zones that acted as barriers. The same behavior has been observed for several other ruptures like the 2005 M_w8.6 Sumatra event (Konca et al., 2008) or the 2010 M_w8.8 Maule event (Contreras-Reyes et al., 2010). The lubricant role of subducting fracture zones was recently proposed for the Lesser Antilles by Schlaphorst et al. (2016), based on *b* value studies. Here we can only conclude that for many fracture zones, we do not detect a specific signal in roughness at any wavelength from 12 to 100 km. However, their intrinsic weakness and potentially high fluid content may certainly play a role in the rupture dynamics during large earthquakes. Further investigations at wavelengths smaller than 12 km in high-resolution mapped areas should be conducted.

5.2. Clear Specific Roughness for Seamounts

Seamounts lend themselves well to roughness investigations especially at short wavelengths (Figure 8). Their roughness amplitude is almost twice the one of a "standard seafloor." Numerous studies in the literature describe the role played by subducting seamounts in stopping or attenuating rupture propagation during large earthquakes off Honshu or Sumatra (e.g., Henstock et al., 2016; Kodaira et al., 2000; Mochizuki et al., 2008). In all these examples, the seamounts were relatively shallow. At larger depths, it is not excluded that subducting seamounts may behave as strong patches during moderate to large earthquakes as proposed beneath the margin off Costa Rica (Bilek et al., 2003; Dominguez et al., 2000). The question of the geodetic coupling associated with subducting seamounts is more debated than their role in seismogenesis, because both strong and weak interseismic coupling have been recorded above subducting seamounts on both sides of the Carnegie Ridge intersecting the north Andean subduction zone (Collot et al., 2017; Marcaillou et al., 2016; Nocquet et al., 2016). Roughness characterization thus appears to be good tool to explore its influence on the seismogenic potential as a function of amplitude or wavelength because earthquakes often nucleate close to some seamounts and then propagate farther, indicating a possible control by the seamount.

5.3. Similar Specific Signature of Seamounts and Ridges at Long Wavelengths

Surprisingly, aseismic ridges cannot be distinguished from the global trend in terms of roughness at short wavelengths (Figure 8). This can be explained by the long wavelength of the ridges themselves, and the fact that they host both seamounts and regular seafloor. At long wavelengths, they share about the same roughness signal in average as the seamounts, covering a large range of roughness values in amplitude. Previous studies have shown that rough seafloor relief, and aseismic ridges in particular, promote creeping rather than seismic coupling (e.g., Kelleher & McCann, 1976; Wang & Bilek, 2014). The reason would be the development of a broad fracture network damaging the upper plate in a similar way as a seamount (Dominguez, Lallemand, Malavieille, & von Huene, 1998; Dominguez et al., 2000) but at a larger scale. Looking in more detail, we often observe a clear positive signal in the roughness for narrow ridges and a very tiny signal for broad ridges (Nazca, Carnegie, or Cocos Ridge, for example, which size exceeds the window size), suggesting that narrow ridges have the same characteristics as seamounts.

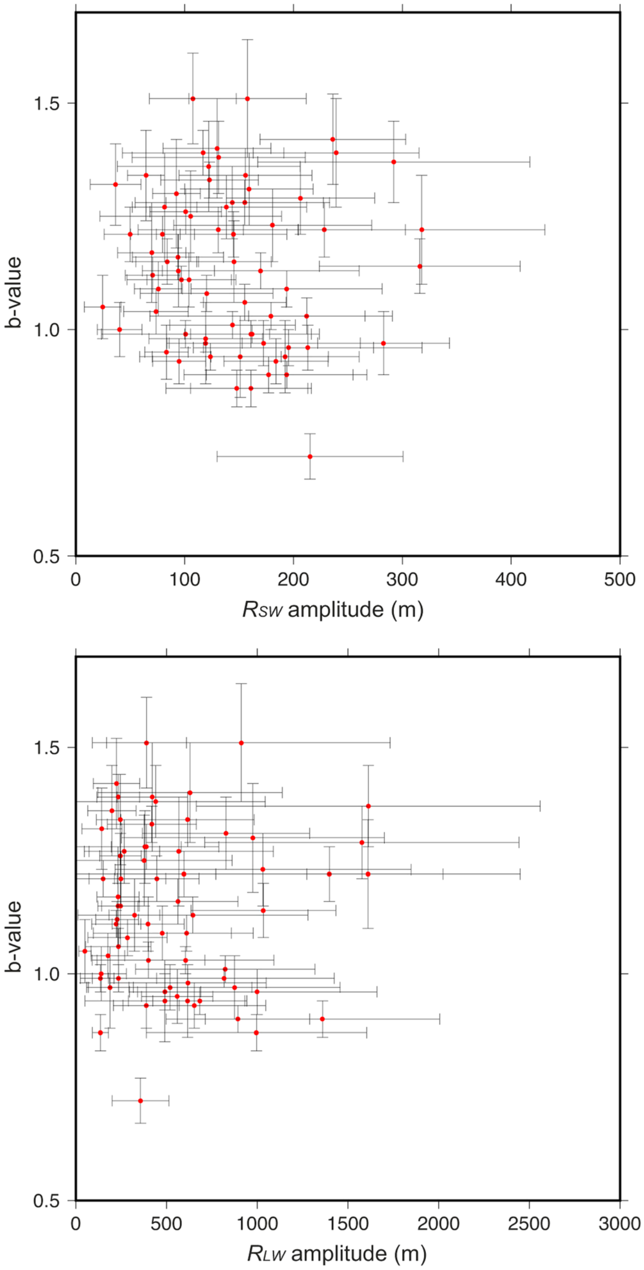

Figure 11. Distribution of roughness values of seafloor facing regions characterized by different *b* values as calculated by Nishikawa and Ide (2014). Standard deviations of roughness values over the wide sampled areas are plotted together with those provided for the *b* values.

5.4. To What Extent can we Classify the Subduction Zones With Respect to Roughness Characteristics?

An important asset of the SubRough database is the possibility to compare any subduction zone with another. We have classified them into three groups from dominantly rough to dominantly smooth (see section 3.2) based on the ratio of low to high R_{LW} amplitudes over given trench segments. For practical reasons, we have proceeded trench by trench. Such sampling is somewhat arbitrary because the same trench can host rough and smooth sections, especially in the mixed group (Table 1; Figure 5). We have thus simplified the purpose in previous section 3.2, but the detailed description trench by trench remains valid, especially when analyzing the lateral variations in roughness amplitudes (Figures 6, 7, and S7 to S12).

5.5. Smooth Areas and Roughness Complexities

The coincidence between thick trench fill and high potential of mega-ruptures has been mentioned by several authors (e.g., Heuret et al., 2012; Ruff, 1989; Scholl et al., 2015). Assuming that the thick trench fill is mostly subducted and then smoothens the plate interface, which is not necessarily verified, authors conclude that a smooth plate boundary enhances seismic coupling and/or rupture propagation. In this study, we have made the choice to remove the contribution from the trench fill by exploring the seafloor at a distance of more than 10 km seaward of the trench, because we considered that part of or even all the trench fill material could be accreted at the front of the margin. We thus focus on the flatness of the subducting seafloor without any contribution from sediment supply in the trench (except if trench fill extends farther than 10 km away from the trench). The lateral extent of the smooth areas is indicated as horizontal lines along each profile in Figures 6, 7, and S7 to S12 (solid line if $R < 100$ m, dotted line if $R < 250$ m; see figure captions for more details). It is clear from Figures 7 and S7 that all trenches belonging to the “rough group” do not show large smooth areas, except locally (lateral extent less than 250 km) along the Mariana Trench. The smoothest seafloor is observed off Andaman, northern Sumatra, Antilles, Cascadia, Japan, Kamchatka, Eastern Aleutians, Western Alaska, Peru, Chile, and Central America. Many of these regions have hosted $M > 8.5$ giant earthquakes (yellow stars in Figures 6, S10, and S12). The lateral extent of the smooth area should play a major role, if we consider that seamounts, ridges, and fracture zones rather act as barriers or sources for rupture complexities. A recent study by Ye et al. (2018) suggested that earthquake complexity was primarily controlled by persistent geological factors. They have quantified the rupture complexity, using the excess radiated energy with respect to the minimum radiated energy expected for a similar source Radiated Energy Enhancement Factor (REEF) for 119 $M_{\mathrm{w}} > 7.0$ earthquakes. A careful comparison between REEF and roughness characteristics would allow to better characterize the nature of the permanent geological features. Corbi et al. (2017) have demonstrated experimentally that the synchronization of slip patches to produce large events depends on the ratio of weak (barrier) to strong (asperity) patches sizes. In their analog experiments, they observed that the barrier became permanent if its size was at least half the size of the asperities. If a link exists between the roughness of the subduction interface and its seismogenic potential (asperity vs barrier), this might explain why the South Chile, Japan-Kuril, Eastern Aleutians-Alaska, or Cascadia, where the proportion of rough to smooth lengths is often less than 0.5, are regions hosting mega-earthquakes. Further analyses are performed to better evaluate those ratios as well as the threshold values in roughness amplitudes (van Rijsingen et al., 2018).

5.6. Roughness and State of Stress in Subduction Zones

It has been observed in some regions that the interseismic coupling, estimated by using geodetic measurements mainly onshore, was partly controlled by the roughness of the subduction interface (e.g., Collot et al., 2017; Nocquet et al., 2016; Yokota et al., 2016), even if no general law can be proposed between a given subducting relief type and its associated degree of coupling. We thus expected some trend by comparing the roughness characteristics of the seismogenic zone proxy with the *b* value or the seismic coupling. The lack of correlation with the *b* value may be due to the width of the sampled area (500 km × 250 km), which reduces the signal by averaging it (see the large error bars in *R* values in Figure 11). The correlation with the seismic coupling is more satisfying, since relatively rough subducting seafloor is always associated with low seismic coupling and high seismic coupling is always associated with relatively smooth subducting seafloor (Figure 10). The seismic coupling coefficient is only indicative because it depends on earthquake recurrence for very large events, which is a function of the degree of coupling and the subduction (loading) rate. It means that we underestimate the seismic coupling in slow subductions (like Antilles) or in regions characterized by earthquake supercycles (Herrendörfer et al., 2015; Nocquet et al., 2016). Despite this approximation, we still observe a clear correlation between high interseismic coupling and low roughness, which is something expected if we consider that creeping is more characteristic of rough subduction interfaces, as proposed by Wang and Bilek (2014).

The subduction of prominent seamount chains, like the D'Entrecasteaux Zone (Vanuatu) or the Louisville Ridge (Tonga) has been described as synchronous with active shortening in the volcanic arc region (Collot et al., 1985; Lallemand et al., 1990; Pelletier et al., 1998). We thus expected that large subducting features might also contribute in upper plate compressive stress. Our statistical analysis apparently does not support such correlation with upper plate stress as a rule. This may indicate that the roughness of the subducting seafloor mainly affects the nearby area of the plate interface even if it contributes in a few regions to the upper plate stress.

5.7. Limitations and Perspectives of the Study

As discussed in section 2.3.2.5, we are fully aware that the unsubducted seafloor is only a proxy of the seismogenic zone and does not represent its exact replica. Seafloor roughness anisotropy and mass transfers between the subducting and overriding plate during the subduction process certainly alter in some way the correlation between the two areas, subsequently diminishing the expected signal. Our computational method does not make the difference between positive and negative reliefs (equation (1)). It is then possible that subducting lows like grabens will be filled by material from the upper plate during the subduction process and will finally produce a smooth subduction interface. However, such lows do not contribute much in the roughness because the reference surface, used for calculating the relative bathymetry, is estimated from a bathymetric grid where seamounts and ridges are removed, so that the positive features dominate the signal. Finally, the comparison of the seafloor roughness along most oceanic subduction zones provides a good basis for addressing numerous studies related to the dynamics of subduction. Building on the good correlation between seafloor roughness and seismic coupling, van Rijsingen et al. (2018) have performed a detailed analysis based on a newly compiled ruptures catalog for 1900–2017 $M_w \geq 7.5$ earthquakes.

6. Conclusion

In this study, we provide a new seafloor roughness database, called SubRough, that allow to characterize the seafloor prior to subduction along most oceanic trenches. Based on R_{LW} amplitude, we propose a classification of the seafloor segments adjacent to subduction zones from dominantly rough to dominantly smooth. The investigated regions can be used as proxies of the adjacent seismogenic zones and thus provide constraints to better understand the seismicity pattern, especially for large to great earthquakes, where rupture complexities or slip patches synchronizations often occur. Large seamounts and ridge flanks mainly contribute in the high roughness character, which in turn is associated with regions of low seismic coupling. Conversely, high seismic coupling is mainly observed in regions characterized by smooth seafloor.

Acknowledgments
We are grateful to Louis Dargère who first explored the various methods used for characterizing the seafloor roughness during his master studies in 2010–2012. This study was supported by CNRS-INSU funding through SYSTER program. It has benefited from discussions with Anthony Sladen, Stéphane Dominguez, Francesca Funiciello, and Fabio Corbi. We are extremely grateful toward Kelin Wang and an anonymous reviewer for the accuracy of their comments and suggestions. The data supporting the conclusions can be obtained in the supporting information with additional material: http://www.gm.univ-montp2.fr/lallemand/Supp_material_G3_roughness_Lallemand.zip

References

Abercrombie, R. E., Antolik, M., Felzer, K., & Ekström, G. (2001). The 1994 java tsunami earthquake: Slip over a subducting seamount. *Journal of Geophysical Research*, *106*, 6595–6607. https://doi.org/10.1029/2000JB900403

Bassett, D., Sandwell, D. T., Fialko, Y., & Watts, A. B. (2016). Upper-plate controls on co-seismic slip in the 2011 magnitude 9.0 Tohoku-oki earthquake. *Nature*, *531*(7592), 92–96. https://doi.org/10.1038/nature16945

Bassett, D., & Watts, A. B. (2015a). Gravity anomalies, crustal structure, and seismicity at subduction zones: 1. Seafloor roughness and subducting relief. *Geochemistry, Geophysics, Geosystems*, *16*, 1508–1540. https://doi.org/10.1002/2014GC005684

Bassett, D., & Watts, A. B. (2015b). Gravity anomalies, crustal structure, and seismicity at subduction zones: 2. Interrelationships between forearc structure and seismogenic behavior. *Geochemistry, Geophysics, Geosystems*, *16*, 1541–1576. https://doi.org/10.1002/2014GC005685

Becker, J. J., Sandwell, D. T., Smith, W. H. F., Braud, J., Binder, B., Depner, J., et al. (2009). Global bathymetry and elevation data at 30 arc seconds resolution: SRTM30_PLUS. *Marine Geodesy*, *32*(4), 355–371. https://doi.org/10.1080/01490410903297766

Bilek, S. L. (2009). Seismicity along the south American subduction zone: Large earthquakes, tsunamis, and subduction zone complexity. *Tectonophysics*. https://doi.org/10.1016/j.tecto.2009.02.037

Bilek, S. L. (2010). Invited review paper: Seismicity along the south American subduction zone: Review of large earthquakes, tsunamis, and subduction zone complexity. *Tectonophysics*, *495*(1-2), 2–14. https://doi.org/10.1016/j.tecto.2009.02.037.

Bilek, S. L., Schwarz, S. Y., & DeShon, H. R. (2003). Control of seafloor roughness on earthquake rupture behavior. *Geology*, *31*(5), 455–458. https://doi.org/10.1130/0091-7613(2003)031<0455:COSROE>2.0.CO;2

Bletery, Q., Thomas, A. M., Rempel, A. W., Karlstrom, L., Sladen, A., & De Barros, L. (2016). Mega-earthquakes rupture flat megathrusts. *Science*, *354*(6315), 1027–1031. https://doi.org/10.1126/science.aag0482

Brune, J. N. (1968). Seismic moment, seismicity, and rate of slip along major fault zones. *Journal of Geophysical Research*, *73*, 777–784. https://doi.org/10.1029/JB073i002p00777

Carena, S. (2011). Subducting-plate topography and nucleation of great and giant earthquakes along the South American trench. *Seismological Research Letters*, *82*(5), 629–637. https://doi.org/10.1785/gssrl.82.5.629

Chlieh, M., Perfettini, H., Tavera, H., Avouac, J.-P., Remy, D., Nocquet, J.-M., et al. (2011). Interseismic coupling and seismic potential along the Central Andes subduction zone. *Journal of Geophysical Research*, *116*, B12405. https://doi.org/10.1029/2010JB008166

Cloos, M. (1992). Thrust-type subduction-zone earthquakes and seamount asperities: A physical model for seismic rupture. *Geology*, *20*(7), 601–604. https://doi.org/10.1130/0091-7613(1992)020<0601:TTSZEA>2.3.CO;2

Collot, J.-Y., Daniel, J., & Burne, R. V. (1985). Recent tectonics associated with the subduction of the D'Entrecasteaux zone in the central new Hebrides. *Tectonophysics*, *112*(1-4), 325–356. https://doi.org/10.1016/0040-1951(85)90185-4

Collot, J.-Y., Lewis, K., Lamarche, G., & Lallemand, S. (2001). The giant Ruatoria debris avalanche on the northern Hikurangi margin, New Zealand: Result of oblique seamount subduction. *Journal of Geophysical Research*, *106*, 19,271–19,297. https://doi.org/10.1029/2001JB900004

Collot, J.-Y., Sanclemente, E., Nocquet, J.-M., Leprêtre, A., Ribodetti, A., Jarrin, P., et al. (2017). Subducted oceanic relief locks the shallow megathrust in Central Ecuador. *Journal of Geophysical Research: Solid Earth*, *122*, 3286–3305. https://doi.org/10.1002/2016JB013849

Contreras-Reyes, E., Flueh, E. R., & Grevemeyer, I. (2010). Tectonic control on sediment accretion and subduction off south Central Chile: Implications for coseismic rupture processes of the 1960 and 2010 megathrust earthquakes. *Tectonics*, *29*, TC6018. https://doi.org/10.1029/2010TC002734

Corbi, F., Funiciello, F., Brizzi, S., Lallemand, S., & Rosenau, M. (2017). Control of asperities size and spacing on seismic behavior of subduction megathrusts. *Geophysical Research Letters*, *44*, 8227–8235. https://doi.org/10.1002/2017GL074182

Corbi, F., Funiciello, F., Faccenna, C., Ranalli, G., & Heuret, A. (2011). Seismic variability of subduction thrust faults: Insights from laboratory models. *Journal of Geophysical Research*, *116*, B06304. https://doi.org/10.1029/2010JB007993

Das, S., & Watts, A. B. (2009). Effect of subducting seafloor topography on the rupture characteristics of great subduction zone earthquakes. In S. Lallemand & F. Funiciello (Eds.), *Subduction Zone Geodynamics* (pp. 103–118). Berlin, Heidelberg: Springer-Verlag. https://doi.org/10.1007/978-3-540-87974-9

Deschamps, A., & Lallemand, S. (2002). The west Philippine Basin: A Paleocene-Oligocene backarc basin opened between two opposed subduction zones. *Journal of Geophysical Research*, *107*(B12), 2322. https://doi.org/10.1029/2001JB001706

Deschamps, A. E., Lallemand, S. E., & Collot, J.-Y. (1998). A detailed study of the Gagua Ridge: A fracture zone ridge uplifted during a plate reorganisation in the mid-Eocene. *Marine Geophysical Researches*, *20*(5), 403–423.

Dominguez, S., Lallemand, S., Malavieille, J., & Schnürle, P. (1998). Oblique subduction of the Gagua ridge beneath the Ryukyu accretionary wedge system: Insights from marine observations and sandbox experiments. *Marine Geophysical Researches*, *20*(5), 383–402. https://doi.org/10.1023/A:1004614506345

Dominguez, S., Lallemand, S. E., Malavieille, J., & von Huene, R. (1998). Upper plate deformation associated with seamount subduction. *Tectonophysics*, *293*(3-4), 207–224. https://doi.org/10.1016/S0040-1951(98)00086-9

Dominguez, S., Malavieille, J., & Lallemand, S. E. (2000). Deformation of accretionary wedges in response to seamount subduction: Insights from sandbox experiments. *Tectonics*, *19*, 182–196. https://doi.org/10.1029/1999TC900055

Dunham, E. M., Belanger, D., Cong, L., & Kozdon, J. E. (2011). Earthquake ruptures with strongly rate-weakening friction and off-fault plasticity, part 2: Nonplanar faults. *Bulletin of Seismological Society of America*, *101*(5), 2308–2322. https://doi.org/10.1785/0120100076

Fisher, M. A., Collot, J.-Y., & Geist, E. L. (1991). Structure of the collision zone between Bougainville Guyot and the accretionary wedge of the new Hebrides island arc, Southwest Pacific. *Tectonics*, *10*, 887–903. https://doi.org/10.1029/91TC00860

Fox, C. G., & Hayes, D. E. (1985). Quantitative methods for analyzing the roughness of the seafloor. *Reviews of Geophysics*, *23*, 1–48. https://doi.org/10.1029/RG023i001p00001

Gao, X., & Wang, K. (2014). Strength of stick-slip and creeping subduction megathrusts from heat flow observations. *Science*, *345*(6200), 1038–1041. https://doi.org/10.1126/science.1255487

Geersen, J., Ranero, C. R., Barckhausen, U., & Reichert, C. (2015). Subducting seamounts control interpolate coupling and seismic rupture in the 2014 Iquique earthquake area. *Nature Communications*, *6*(1), 8267. https://doi.org/10.1038/ncomms9267

Gutenberg, B., & Richter, C. F. (1944). Frequency of earthquakes in California. *Bulletin of the Seismological Society of America*, *34*, 185–188.

Gutscher, M.-A., Malavieille, J., Lallemand, S., & Collot, J.-Y. (1999). Tectonic segmentation of the north Andean margin: Impact of the Carnegie ridge collision. *Earth and Planetary Science Letters*, *168*(3-4), 255–270. https://doi.org/10.1016/S0012-821X(99)00060-6

Gutscher, M.-A., Spakman, W., Bijwaard, H., & Engdahl, E. R. (2000). Geodynamics of flat subduction: Seismicity and tomographic constraints from the Andean margin. *Tectonics*, *9*, 814–833. https://doi.org/10.1029/1999TC001152

Gutscher, M.-A., & Westbrook, G. K. (2009). Great earthquakes in slow-subduction, low-taper margins. In S. Lallemand, & F. Funiciello (Eds.), *Subduction Zone Geodynamics* (pp. 119–133). Berlin, Heidelberg: Springer-Verlag. https://doi.org/10.1007/978-3-540-87974-9

Henstock, T. J., McNeill, L. C., Bull, J. M., Cook, B. J., Gulick, P. S., Austin, J. A., et al. (2016). Downgoing plate topography stopped rupture in the A.D. 2005 Sumatra earthquake. *Geology*, *44*(1), 71–74. https://doi.org/10.1130/G37258.1

Herrendörfer, R., van Dinther, Y., Gerya, T., & Dalguer, L. A. (2015). Earthquake supercycle in subduction zones controlled by the width of the seismogenic zone. *Nature Geoscience*. https://doi.org/10.1038/NGEO2427, *8*(6), 471–474.

Heuret, A., Conrad, C. P., Funiciello, F., Lallemand, S., & Sandri, L. (2012). Relation between subduction megathrust earthquakes, trench sediment thickness and upper plate strain. *Geophysical Research Letters*, *39*, L05304. https://doi.org/10.1029/2011GL050712

Heuret, A., & Lallemand, S. (2005). Plate motions, slab dynamics and back-arc deformation. *Physics of the Earth and Planetary Interiors*, *149*(1-2), 31–51. https://doi.org/10.1016/j.pepi.2004.08.022

Heuret, A., Lallemand, S., Funiciello, F., Piromallo, C., & Faccenna, C. (2011). Physical characteristics of subduction interface type seismogenic zones revisited. *Geochemistry, Geophysics, Geosystems*, *12*, Q01004. https://doi.org/10.1029/2010GC003230

Huang, J., & Turcotte, D. L. (1989). Fractal mapping of digitized images: Application to the topography of Arizona and comparisons with synthetic images. *Journal of Geophysical Research*, *94*, 7491–7495. https://doi.org/10.1029/JB094iB06p07491

Huang, J., & Turcotte, D. L. (1990). Are earthquakes an example of deterministic chaos? *Geophysical Research Letters*, *17*, 223–226. https://doi.org/10.1029/GL017i003p00223

Ide, S. (2010). Striations, duration, migration and tidal response in deep tremor. *Nature*, *466*(7304), 356–359. https://doi.org/10.1038/nature09251

Ishizuka, O., Taylor, R. N., Ohara, Y., & Yuasa, M. (2013). Upwelling, rifting, and age-progressive magmatism from the Oki-Daito mantle plume. *Geology*, *41*(9), 1011–1014. https://doi.org/10.1130/G34525.1

Jarrard, R. D. (1986). Relations among subduction parameters. *Reviews of Geophysics*, *24*, 217–284. https://doi.org/10.1029/RG024i002p00217

Kelleher, J., & McCann, W. (1976). Buoyant zones, great earthquakes, and unstable boundaries of subduction. *Journal of Geophysical Research*, *81*, 4885–4896. https://doi.org/10.1029/JB081i026p04885

Kim, S.-S., & Wessel, P. (2011). New global seamount census from altimetry-derived gravity data. *Geophysical Journal International*, *186*(2), 615–631. https://doi.org/10.1111/j.1365-246X.2011.05076.x

Kodaira, S., Takahashi, N., Nakanishi, A., Miura, S., & Kaneda, Y. (2000). Subducted seamount imaged in the rupture zone of the 1946 Nankaido earthquake. *Science*, *289*(5476), 104–106. https://doi.org/10.1126/science.289.5476.104.

Konca, A. O., Avouac, J.-P., Sladen, A., Meltzner, A. J., Sieh, K., Fang, P., et al. (2008). Partial rupture of a locked patch of the Sumatra megathrust during the 2007 earthquake sequence. *Nature*, *456*(7222), 631–635. https://doi.org/10.1038/nature07572.

Kopp, H. (2013). Invited review paper: The control of subduction zone structural complexity and geometry on margin segmentation and seismicity. *Tectonophysics*, *589*, 1–16. https://doi.org/10.1016/j.tecto.2012.12.037

Laigle, M., Becel, A., de Voogd, B., Sachpazi, M., Bayrakci, G., Lebrun, J.-F., et al. (2013). Along-arc segmentation and interactions of subducting ridges with the Lesser Antilles subduction forearc crust revealed by MCS imaging. *Tectonophysics*, *603*, 32–54. https://doi.org/10.1016/j.tecto.2013.05.028

Lallemand, S. (2016). (2016). Philippine Sea plate inception, evolution and consumption with special emphasis on the early stages of Izu-Bonin-Mariana subduction. *Progress in Earth and Planetary Science*, *3*(1), 1–27. https://doi.org/10.1186/s40645-016-0085-6

Lallemand, S., Collot, J.-Y., Pelletier, B., Rangin, C., & Cadet, J.-P. (1990). Impact of oceanic asperities on the tectogenesis of modern convergent margins. *Oceanologica Acta*, *10*, 17–30.

Lallemand, S., Culotta, R., & von Huene, R. (1989). Subduction of the Daiichi Kashima seamount in the Japan trench. *Tectonophysics*, *160*(1-4), 231–247. https://doi.org/10.1016/0040-1951(89)90393-4

Lallemand, S. E., Malavieille, J., & Calassou, S. (1992). Effects of oceanic ridge subduction on accretionary wedges: Experimental modeling and marine observations. *Tectonics*, *11*, 1301–1313. https://doi.org/10.1029/92TC00637

Lallemand, S. E., Schnurle, P., & Malavieille, J. (1994). Coulomb theory applied to accretionary and non-accretionary wedges: Possible causes for tectonic erosion and/or frontal accretion. *Journal of Geophysical Research*, *99*, 12,033–12,055. https://doi.org/10.1029/94JB00124

Landgrebe, T. C. W., & Müller, R. D. (2015). Uncovering the relationship between subducting bathymetric ridges and volcanic chains with significant earthquakes using geophysical data mining. *Australian Journal of Earth Sciences*, *62*(2), 171–180. https://doi.org/10.1080/08120099.2015.1003145

Lewis, K., Lallemand, S., & Carter, L. (2004). Collapse in a quaternary shelf basin off east cape, New Zealand: Evidence for passage of a subducted seamount inboard of the Ruatoria giant avalanche. *New Zealand Journal of Geology and Geophysics*, *47*(3), 415–429. https://doi.org/10.1080/00288306.2004.9515067

Lewis, K. B., Collot, J.-Y., & Lallemand, S. E. (1998). The dammed Hikurangi trough: A channel-fed trench blocked by subducting seamounts and their wake avalanches (New Zealand–France GeodyNZ project). *Basin Research*, *10*(4), 441–468. https://doi.org/10.1046/j.1365-2117.1998.00080.x

Lin, W., Conin, M., Moore, J. C., Chester, F. M., Nakamura, Y., Mori, J. J., et al. (2013). Stress state in the largest displacement area of the 2011 Tohoku-Oki earthquake. *Science*, *339*, 687–690. https://doi.org/10.1126/science.1229379

Marcaillou, B., Collot, J.-Y., Ribodetti, A., d'Acremont, E., Mahamat, A.-A., & Alvarado, A. (2016). Seamount subduction at the north-Ecuadorian convergent margin: Effects on structures, inter-seismic coupling and seismogenesis. *Earth and Planetary Science Letters*, *433*, 146–158. https://doi.org/10.1016/j.epsl.2015.10.043

McCaffrey, R. (2008). Global frequency of magnitude 9 earthquakes. *Geology*, *36*(3), 263–266. https://doi.org/10.1130/G24402A.1

Métois, M., Socquet, A., & Vigny, C. (2012). Interseismic coupling, segmentation and mechanical behavior of the Central Chile subduction zone. *Journal of Geophysical Research*, *117*, B03406. https://doi.org/10.1029/2011JB008736

Mochizuki, K., Yamada, T., Shinohara, M., Yamanaka, Y., & Kanazawa, T. (2008). Weak interplate coupling by seamounts and repeating M-7 earthquakes. *Science*, *321*, 1195–1197.

Moeremans, R. E., & Singh, S. C. (2014). Seismic evidence of continental margin influence on the NinetyEast ridge in the bay of Bengal. *Geophysical Research Letters*, *41*, 7143–7150. https://doi.org/10.1002/2014GL061598

Morgan, E. C., McAdoo, B. G., & Baise, L. G. (2008). Quantifying geomorphology associated with large subduction zone earthquakes. *Basin Research*, *20*(4), 531–542. https://doi.org/10.1111/j.1365-2117.2008.00368.x.

Müller, R. D., & Landgrebe, T. C. W. (2012). The link between great earthquakes and the subduction of oceanic fracture zones. *Solid Earth*, *3*(2), 447–465. https://doi.org/10.5194/se-3-447-2012.

Nishikawa, T., & Ide, S. (2014). Earthquake size distribution in subduction zones linked to slab buoyancy. *Nature Geoscience*, *7*(12), 904–908. https://doi.org/10.1038/NGEO2279.

Nocquet, J.-M., Jarrin, P., Vallée, M., Mothes, P. A., Grandin, R., Rolandone, F., et al. (2016). Supercycle at the Ecuadorian subduction zone revealed after the 2016 Pedernales earthquake. *Nature Geoscience*, *10*(2), 145–149. https://doi.org/10.1038/NGEO2864.

Park, J. O., Hori, T., & Kaneda, Y. (2009). Seismotectonic implications of the Kyushu-Palau ridge subducting beneath the westernmost Nankai forearc. *Earth, Planets and Space*, *61*(8), 1013–1018. https://doi.org/10.1186/BF03352951

Pedley, K. L., Barnes, P. M., Pettinga, J. R., & Lewis, K. B. (2010). Seafloor structural geomorphic evolution of the accretionary frontal wedge in response to seamount subduction, poverty indentation, New Zealand. *Marine Geology*, *270*(1-4), 119–138. https://doi.org/10.1016/j.margeo.2009.11.006.

Pelletier, B., Calmant, S., & Pillet, R. (1998). Current tectonics of the Tonga-new Hebrides region. *Earth and Planetary Science Letters*, *164*(1-2), 263–276. https://doi.org/10.1016/S0012-821X(98)00212-X

Pelletier, B., & Dupont, J. (1990). Effets de la subduction de la Ride de Louisville sur l'arc des Tonga-Kermadec. *Oceanologica Acta*, *10*, 56–76. (in French with English abstract)

Perron, J. T., Kirchner, J. W., & Dietrich, W. E. (2008). Spectral signature of characteristic spatial scales and nonfractal structures in landscapes. *Journal of Geophysical Research*, *113*, F04003. https://doi.org/10.1029/2007JF000866

Peterson, E. T., & Seno, T. (1984). Factors affecting seismic moment release rates in subduction zones. *Journal of Geophysical Research*, *89*, 10,233–10,248. https://doi.org/10.1029/JB089iB12p10233

Ranero, C., & von Huene, R. (2000). Subduction erosion along the middle America convergent margin. *Nature*, *404*(6779), 748–752. https://doi.org/10.1038/35008046

Ranero, C. R., Grevemeyer, I., Sahling, H., Barckhausen, U., Hensen, C., Wallmann, K., et al. (2008). Hydrogeological system of erosional convergent margins and its influence on tectonics and interplate seismogenesis. *Geochemistry, Geophysics, Geosystems*, *9*, Q03S04. https://doi.org/10.1029/2007GC001679

Renard, F., Candela, T., & Bouchaud, E. (2013). Constant dimensionality of fault roughness from the scale of micro-fractures to the scale of continents. *Journal of Geophysical Research*, *40*, 83–87. https://doi.org/10.1029/2012GL054143

Robinson, D. P., Das, S., & Watts, A. B. (2006). Earthquake rupture stalled by a subducting fracture zone. *Science*, *312*(5777), 1203. https://doi.org/10.1126/science.1125771–1205.

Rodriguez, M., Chamot-Rooke, N., Fournier, M., Huchon, P., & Delescluse, M. (2013). Mode of opening of an oceanic pull-apart: The 20°N Basin along the Owen Fracture Zone (NW Indian Ocean). *Tectonics*, *32*, 1343–1357. https://doi.org/10.1002/tect.20083

Ruff, L. (1989). Do trench sediments affect great earthquake occurrence in subduction zones? *Pure and Applied Geophysics*, *129*(1-2), 263–282. https://doi.org/10.1007/BF00874629

Ruff, L., & Kanamori, H. (1983). Seismic coupling and uncoupling at subduction zones. *Tectonophysics*, *99*(2-4), 99–117. https://doi.org/10.1016/0040-1951(83)90097-5

Ruff, L. J. (1992). Asperity distributions and large earthquake occurrence in subduction zones. *Tectonophysics*, *211*(1-4), 61–83. https://doi.org/10.1016/0040-1951(92)90051-7

Saffer, D. M., & Tobin, H. J. (2011). Hydrogeology and mechanics of subduction zone forearcs: Fluid flow and pore pressure. *Annual Review of Earth and Planetary Sciences*, *39*(1), 157–186. https://doi.org/10.1146/annurev-earth-040610-133408.

Sage, F., Collot, J.-Y., & Ranero, C. R. (2006). Interplate patchiness and subduction-erosion mechanisms: Evidence from depth-migrated seismic images at the Central Ecuador convergent margin. *Geology*, *34*(12), 997–1000. https://doi.org/10.1130/G22790A

Saillard, M., Audin, L., Rousset, B., Avouac, J.-P., Chlieh, M., Hall, S. R., et al. (2017). From the seismic cycle to long-term deformation: Linking seismic coupling and quaternary coastal geomorphology along the Andean megathrust. *Tectonics*, *36*, 241–256. https://doi.org/10.1002/2016TC004156

Sandwell, D. T., Gille, S. T., & Smith, W. H. F. (Eds) (2002). *Bathymetry from space: Oceanography, geophysics, and climate, geoscience professional services* (p. 24). Maryland: Bethesda.

Schellart, W. P., & Rawlinson, N. (2013). Global correlations between maximum magnitudes of subduction zone interface thrust earthquakes and physical parameters of subduction zones. *Physics of the Earth and Planetary Interiors*, *225*, 41–67. https://doi.org/10.1016/j.pepi.2013.10.001

Schlaphorst, D., Kendall, J.-M., Collier, S., Verdon, J. P., Blundy, J., Baptie, B., et al. (2016). Water, oceanic fracture zones and the lubrication of subducting plate boundaries—Insights from seismicity. *Geophysical Journal International*, *204*(3), 1405–1420. https://doi.org/10.1093/gji/ggv509.

Scholl, D. W., Kirby, S. H., von Huene, R., Ryan, H., Wells, R. E., & Geist, E. L. (2015). Great (Mw8.0) megathrust earthquakes and the subduction of excess sediment and bathymetrically smooth seafloor. *Geosphere*, *11*(2), 236–265. https://doi.org/10.1130/GES01079.1

Scholz, C. H. (1998). Earthquakes and friction laws. *Nature*, *391*(6662), 37–42. https://doi.org/10.1038/34097

Scholz, C. H., & Small, C. (1997). The effect of seamount on seismic coupling. *Geology*, *25*(6), 487–490. https://doi.org/10.1130/0091-7613(1997)025<0487:TEOSSO>2.3.CO;2

Singh, S. C., Hananto, N., Mukti, M., Robinson, D. P., Das, S., Chauhan, A., et al. (2011). Aseismic zone and earthquake segmentation associated with a deep subducted seamount in Sumatra. *Nature Geoscience*, *4*(5), 308–311. https://doi.org/10.1038/ngeo1119.

Smith, W. H. F., & Sandwell, D. T. (1997). Global Sea floor topography from satellite altimetry and ship depth soundings. *Science*, *277*, 1957–1962.

Sparkes, R., Tilmann, F., Hovius, N., & Hillier, J. (2010). Subducted seafloor relief stops rupture in south American great earthquakes: Implications for rupture behaviour in the 2010 Maule, Chile earthquake. *Earth and Planetary Science Letters*, *298*(1-2), 89–94. https://doi.org/10.1016/j.epsl.2010.07.029.

Turcotte, D. L. (1992). Fractals, chaos, self-organized criticality and tectonics. *Terra Nova*, *4*(1), 4–12. https://doi.org/10.1111/j.1365-3121.1992.tb00444.x

Turcotte, D. L. (1997). *Fractals and chaos in geology and geophysics*. New York: Cambridge Univ. Press.

Uyeda, S. (1987). Chilean vs. Mariana type subduction zones with remarks on arc volcanism and collision tectonics. In J. W. H. Monger & J. Francheteau (Eds.), *Circum-Pacific orogenic belts and evolution of the Pacific Ocean basin*, *Geodynamics Series 18, Int. Lith. Pr. Contrib* (pp. 1–7). Washington, DC/ Boulder, CO: AGU/GSA. https://doi.org/10.1029/GD018p0001

van Rijsingen, E., Lallemand, S., Peyret, M., Heuret, A., Arcay, D., Funiciello, F., & Corbi, F. (2018). How subduction interface roughness influences the occurrence of large interplate earthquakes. *Geochemistry, Geophysics, Geosystems*, *19*. https://doi.org/10.1029/2018GC007618

von Huene, R., Bialas, J., Flueh, E., Cropp, B., Csernok, T., Fabel, E., et al. (1995). Morphotectonic features of the Costa Rican Pacific margin surveyed during the Sonne 76 cruise. *Geological Society of America Special Papers*, *295*, 291–307. https://doi.org/10.1130/SPE295-p291

von Huene, R., Ranero, C. R., & Vannucchi, P. (2004, 10). Generic model of subduction erosion. *Geology*, *32*, 913–916. https://doi.org/10.1130/G20563.1

von Huene, R., Ranero, C. R., & Weinrebe, W. (2000). Quaternary convergent margin tectonics of Costa Rica, segmentation of the Cocos plate, and central American volcanism. *Tectonics*, *19*, 314–334. https://doi.org/10.1029/1999TC001143

von Huene, R., & Scholl, D. W. (1991). Observations at convergent margins concerning sediment subduction, subduction erosion, and the growth of continental crust. *Reviews of Geophysics*, *29*, 279–316. https://doi.org/10.1029/91RG00969

Voss, R. F. (1988). Fractals in nature: From characterization to simulation. In H. O. Peitgen & D. Saupe (Eds.), *The science of fractal images* (pp. 21–70). New-York: Springer. https://doi.org/10.1007/978-1-4612-3784-6_1

Wallace, L. M., Ellis, S., & Mann, P. (2009). Collisional model for rapid fore-arc block rotations, arc curvature, and episodic back-arc rifting in subduction settings. *Geochemistry, Geophysics, Geosystems*, *10*, Q05001. https://doi.org/10.1029/2008GC002220

Wang, K., & Bilek, S. L. (2011). Do subducting seamounts generate or stop large earthquakes? *Geology*, *39*(9), 819–822. https://doi.org/10.1130/G31856.1

Wang, K., & Bilek, S. L. (2014). Fault creep caused by subduction of rough seafloor relief. *Tectonophysics*, *610*, 1–24. https://doi.org/10.1016/j.tecto.2013.11.024

Weatherall, P., Marks, K. M., Jakobsson, M., Schmitt, T., Tani, S., Arndt, J. E., et al. (2015). A new digital bathymetric model of the world's oceans. *Earth and Space Science*, *2*, 331–345. https://doi.org/10.1002/2015EA000107

Wessel, P. (2001). Global distribution of seamounts inferred from gridded Geosat/ERS-1 altimetry. *Journal of Geophysical Research*, *106*, 19,431–19,441. https://doi.org/10.1029/2000JB000083

Yang, H., Liu, Y., & Lin, J. (2012). Effects of subducted seamounts on megathrust earthquake nucleation and rupture propagation. *Geophysical Research Letters*, *39*, L24302. https://doi.org/10.1029/2012GL053892

Ye, L., Kanamori, H., & Lay, T. (2018). Global variations of large megathrust earthquake rupture characteristics. *Science Advances*, *4*, 1–8. https://doi.org/10.1126/sciadv.aao4915

Yokota, Y., Ishikawa, T., Watanabe, S., Tashiro, T., & Asada, A. (2016). Seafloor geodetic constraints on interplate coupling of the Nankai Trough megathrust zone. *Nature*, *534*(7607), 374–377. https://doi.org/10.1038/nature17632